

Erosional impact on fault segmentation in thrust belts: Low-temperature thermochronology and fluvial shear stress analyses on an aftershock gap along eastern margin of Tibetan Plateau

Xibin Tan¹, Yijia Ye², Yiduo Liu³, Feng Shi⁴, Yuan-Hsi Li⁵, Jiangfei Hou², and Li Qian²

¹Institute of Geology, China Earthquake Administration, Beijing 100029, China

²Institute of Geology, China Earthquake Administration

³University of Houston

⁴State Key Laboratory of Earthquake Dynamics, Institute of Geology, China Earthquake Administration, Beijing 100029, China.

⁵National Chung-Cheng University

November 22, 2022

Abstract

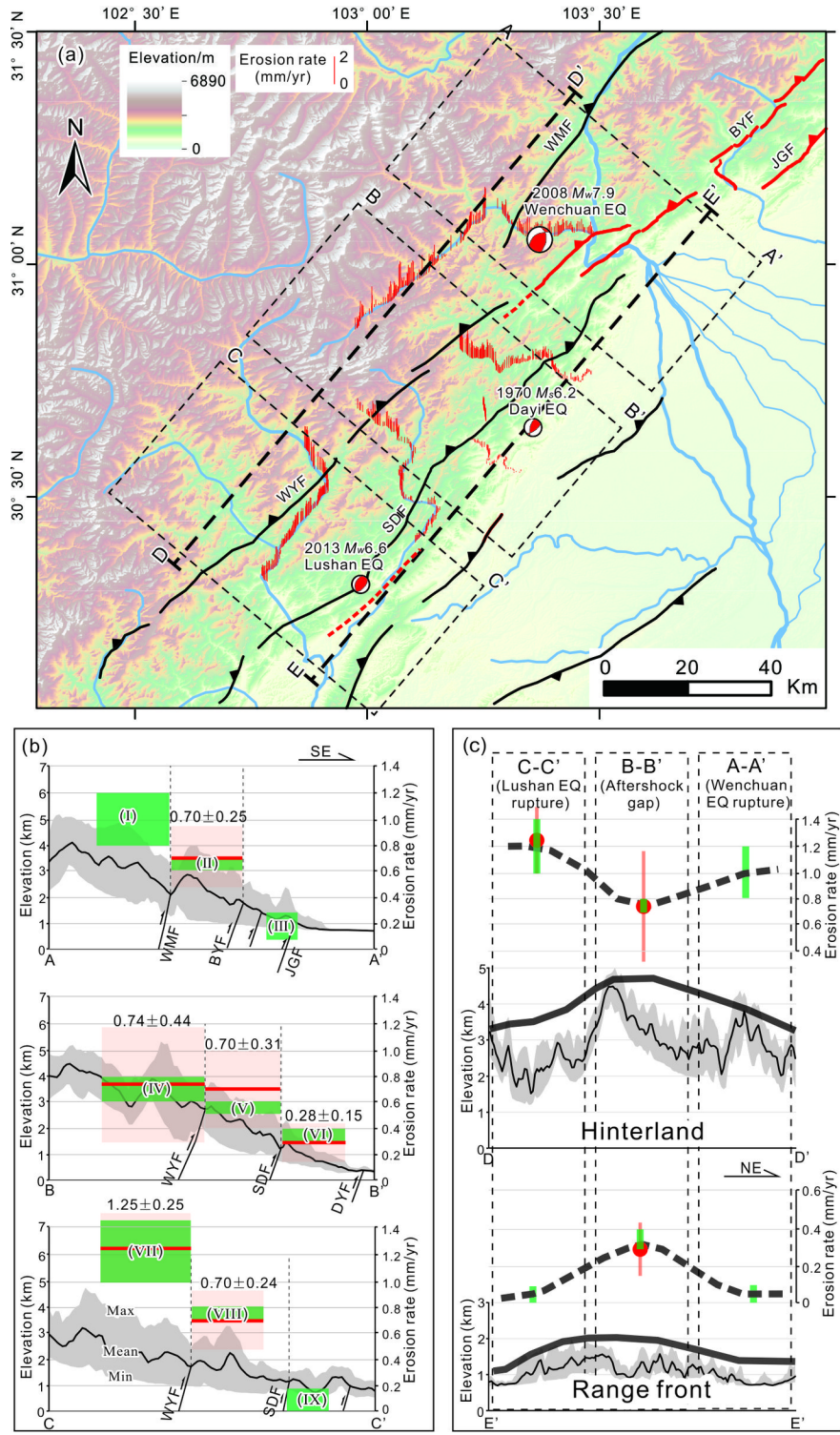
Mechanism for fault segmentation in thrust belt is a key to understanding the orogenic process and seismic risks. A ~50 km long aftershock gap emerged between the ruptures of the 2008 Wenchuan and the 2013 Lushan earthquakes along the eastern margin of the Tibetan Plateau. Previous studies suggested that weak materials under ductile deformation cause the gap. Here we propose an alternative explanation: differential erosion drives the along-strike variation in fault activity. To testify the two competing models, we conducted low-temperature thermochronology and fluvial shear stress analyses to depict the spatial distributions of erosion. We obtained eight apatite fission track dates (6-44 Ma) in the gap and deduced erosion rates of 0.5-0.6 mm/yr and 0.3-0.4 mm/yr since ~8 Ma in the hanging -wall and footwall of the Shuangshi-Dachuan fault, respectively. We carried out linear fitting based on an empirical relationship between thermochronology-derived erosion rate and fluvial shear stress, and then calculated the erosion rate for each survey point of fluvial shear stress. Our new data reveal that in the hinterland, the erosion rate at the gap is lower than that of adjacent areas along strike, whereas in the range front, the erosion rate at the gap is greater. This spatial pattern supports the “differential erosion” hypothesis and is at odds with the “weak material” model. This study illustrates that heterogeneous erosion regulates fault segmentation in this thrust belt. Moreover, the aftershock gap acts as a barrier for the past major earthquakes, which poses substantial seismic potential to this region.

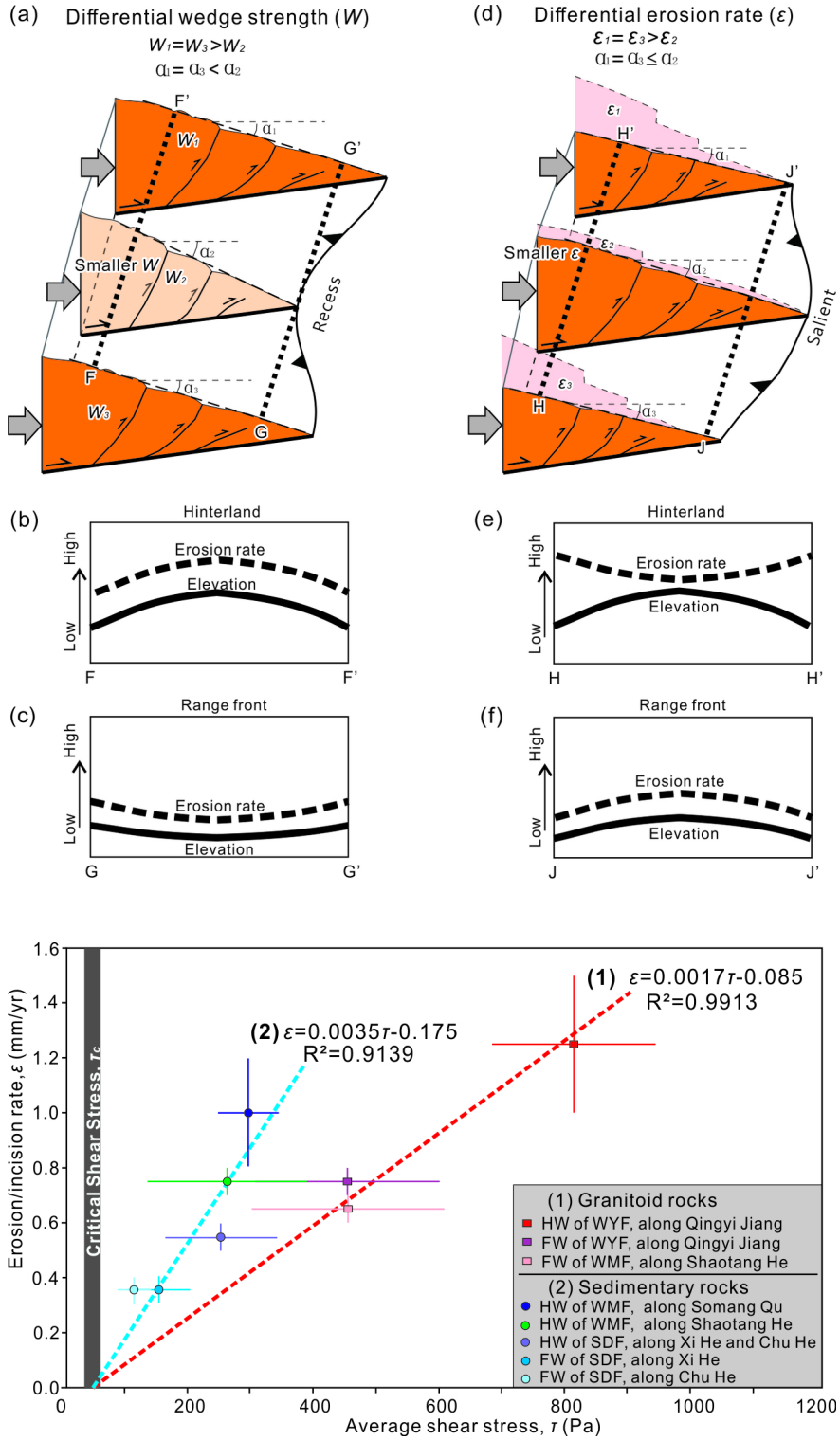
Hosted file

table 1.docx available at <https://authorea.com/users/533309/articles/598159-erosional-impact-on-fault-segmentation-in-thrust-belts-low-temperature-thermochronology-and-fluvial-shear-stress-analyses-on-an-aftershock-gap-along-eastern-margin-of-tibetan-plateau>

Hosted file

table s1.docx available at <https://authorea.com/users/533309/articles/598159-erosional-impact-on-fault-segmentation-in-thrust-belts-low-temperature-thermochronology-and-fluvial-shear-stress-analyses-on-an-aftershock-gap-along-eastern-margin-of-tibetan-plateau>





1 **Erosional impact on fault segmentation in thrust belts:**
2 **Low-temperature thermochronology and fluvial shear stress analyses**
3 **on an aftershock gap along eastern margin of Tibetan Plateau**

4

5 Yijia Ye¹, Xibin Tan^{1,*}, Yiduo Liu², Feng Shi¹, Yuan-Hsi Lee³, Jiangfei Hou¹, and Li Qian¹

6 1 State Key Laboratory of Earthquake Dynamics, Institute of Geology, China Earthquake

7 Administration, Beijing, 100029, China

8 2 Department of Earth and Atmospheric Sciences, University of Houston, Houston, TX,

9 77204-5007, USA

10 3 Department of Earth and Environmental Sciences, National Chung-Cheng University, Chia-Yi,

11 62102, Taiwan

12

13

14 **Abstract**

15 Mechanism for fault segmentation in thrust belt is a key to understanding the
16 orogenic process and seismic risks. A ~50 km long aftershock gap emerged between
17 the ruptures of the 2008 Wenchuan and the 2013 Lushan earthquakes along the
18 eastern margin of the Tibetan Plateau. Previous studies suggested that weak materials
19 under ductile deformation cause the gap. Here we propose an alternative explanation:
20 differential erosion drives the along-strike variation in fault activity. To testify the two
21 competing models, we conducted low-temperature thermochronology and fluvial
22 shear stress analyses to depict the spatial distributions of erosion. We obtained eight
23 apatite fission track dates (6-44 Ma) in the gap and deduced erosion rates of 0.5-0.6
24 mm/yr and 0.3-0.4 mm/yr since ~8 Ma in the hanging -wall and footwall of the
25 Shuangshi-Dachuan fault, respectively. We carried out linear fitting based on an
26 empirical relationship between thermochronology-derived erosion rate and fluvial
27 shear stress, and then calculated the erosion rate for each survey point of fluvial shear
28 stress. Our new data reveal that in the hinterland, the erosion rate at the gap is lower
29 than that of adjacent areas along strike, whereas in the range front, the erosion rate at
30 the gap is greater. This spatial pattern supports the “differential erosion” hypothesis
31 and is at odds with the “weak material” model. This study illustrates that
32 heterogeneous erosion regulates fault segmentation in this thrust belt. Moreover, the
33 aftershock gap acts as a barrier for the past major earthquakes, which poses
34 substantial seismic potential to this region.

35

36

37 **Key Points**

- 38 1. Erosion rates (0.5-0.6 and 0.3-0.4 mm/yr across the Shuangshi-Dachuan fault) in
39 aftershock gap of Longmen Shan.
- 40 2. Spatial pattern of erosion along and across Longmen Shan supports heterogeneous
41 erosion model.
- 42 3. Differential erosion regulates fault segmentation and points to barrier model for
43 Longmen Shan seismicity.

44

45 **1. Introduction**

46 Thrust belt is ubiquitously characterized by segmentation. Most of the fault
47 segmentation results from geometrical and/or lithological changes along fault strike
48 (e.g., [Mazzoli et al., 2005](#); [Jin et al., 2010](#); [C. Sun et al., 2019](#)). Some, however, are
49 controlled by erosion (e.g., [Norris and Copper, 1997](#); [Horton, 1999](#)), a mechanism
50 that is arguably underappreciated. This study introduces a new example of thrust
51 segmentation under erosional control and a method to distinguish such a mechanism.

52 The Longmen Shan range, located along the eastern margin of the Tibetan
53 Plateau, possesses steep relief and active tectonics ([S.F. Chen et al., 1994](#); [Clark and](#)
54 [Royden, 2000](#); [Kirby et al., 2002](#); [Yin et al., 2010](#)). The 2008 M_w 7.9 Wenchuan and
55 2013 M_w 6.6 Lushan earthquakes are the most catastrophic events in recent decades,
56 causing huge casualties and property losses (**Fig. 1**) ([Xu et al., 2009](#); [Shen et al., 2009](#);
57 [Xu et al., 2013](#)). A segment ~50 km long between the ruptures of the 2008 Wenchuan
58 earthquake and the 2013 Lushan earthquake has remained unruptured in both events,
59 and is called an “aftershock gap” ([Pei et al., 2014](#)). To understand the nature of the
60 gap, previous studies focused on the velocity structure of the lithosphere ([Z.W. Li et](#)
61 [al., 2013](#); [Pei et al., 2014](#); [Liang et al., 2018](#)) and paleo-earthquake records on the
62 major faults ([H. Wang et al., 2015](#); [Dong et al., 2017](#); [Shao et al., 2019](#)). Several
63 seismological studies found low-velocity anomalies in the upper crust within the gap,
64 and suggested weak materials that accommodate ductile deformation and inhibit large
65 earthquakes ([Z.W. Li et al., 2013](#); [Pei et al., 2014](#); [Z. Liu et al., 2018](#)). However,
66 low-velocity anomalies are not restricted in this gap; other regions with similar

67 low-velocity zones do not exhibit a seismic or aftershock gap (e.g., [Z. Liu et al., 2018](#)).
68 Moreover, as detailed in Discussion, the “weak material” model would predict
69 morphotectonic features that are inconsistent with the surface geology (**Fig. 1**). Here
70 we propose an alternative hypothesis: differential erosion induced along-strike
71 variations in fault activity, which inhibited the seismic rupture propagation during the
72 Wenchuan and Lushan earthquakes in the gap.

73 While both models can lead to an aftershock gap, their predictions on the spatial
74 distributions of deformation and denudation differ. In the context of the critical-taper
75 wedge theory ([Davis et al., 1983](#); [Suppe, 2007](#)), which is applicable to the Longmen
76 Shan thrust belt ([Hubbard et al., 2010](#)), the first model would result in more intense
77 deformation in the hinterland and weaker deformation at the range front at the
78 aftershock gap than surrounding regions along strike, whereas the second model
79 predicts the opposite scenario ([Y. Liu et al., in review](#)). Denudation pattern is a good
80 proxy to characterizing the deformation patten (e.g., [Tian et al., 2013](#); [Tan et al., 2019](#)),
81 and therefore a useful measure to test the competing mechanisms.

82 In this study, we report eight apatite fission track (AFT) dates in the aftershock
83 gap and perform low-temperature thermochronological modeling using HeFTy (**Fig.**
84 **2a**). We further calculate the fluvial shear stress in rivers within the gap and adjacent
85 portions, as a proxy for incision intensity to gain a wider distribution of erosion (**Fig.**
86 **2b**) ([Lavé and Avouac, 2001](#); [Godard et al., 2010](#)). These results are compared with
87 the predicted deformation and denudation patterns of the competing models, with an
88 attempt to advance our understanding on the segmentation in thrust belts.

90 **2. Geological Setting**

91 The Longmen Shan is located along the eastern margin of the Tibetan Plateau,
92 adjacent to the Sichuan Basin (**Fig. 1**). Within 50 km of distance across the Longmen
93 Shan, the mean elevation ascends dramatically from ~500 m in the Sichuan Basin to
94 over 5,000 m above sea level in the Tibetan Plateau, forming the steepest topographic
95 gradient in the Tibetan Plateau region and, arguably, of the world (Clark & Royden,
96 2000; Kirby et al., 2002). Four tectonostratigraphic units exist in the Longmen Shan,
97 including: (1) Precambrian crystalline basement of gneisses and granitoids; (2)
98 Neoproterozoic-Permian passive margin sedimentary sequence; (3) Triassic flysch
99 sequence in the Songpan-Ganze terrane of the Tibetan Plateau; and (4)
100 Mesozoic-Cenozoic sedimentary rocks in the Yangtze Craton of the South China
101 Block (Burchfiel et al., 1995; Kirby et al., 2002).

102 The Longmen Shan is a reactivated orogen (Jia et al., 2006; M. Sun et al., 2018;
103 Tan et al., 2019). It was an intra-continental fold-and-thrust belt during the Mesozoic,
104 accommodating transpressional convergence between the Songpan-Ganze terrane and
105 the Yangtze Craton (Burchfiel et al., 1995; de Sigoyer et al., 2014). In the Cenozoic,
106 following the Indian-Eurasian collision (Royden et al., 1997; Yin and Harrison, 2000;
107 Tapponnier et al., 2001), the outward growth of the Tibetan Plateau reactivated many
108 faults along the eastern Tibetan Plateau margin; collectively, they form the Longmen
109 Shan thrust belt (**Fig. 1**).

110 The northeast-trending Longmen Shan thrust belt (500 km long and 30-60 km
111 wide) consists of several sub-parallel, NW-dipping thrust faults. From northwest to
112 southeast in the central segment, the faults are Wenchuan-Maoxian (WMF),
113 Beichuan-Yingxiu (BYF), and Jiangyou-Guanxian fault, respectively. Sub-parallel
114 major thrust faults are also present in the southern Longmen Shan, including the
115 Wulong-Yanjing fault (WYF) and the Shuangshi-Dachuan fault (SDF) (**Fig. 1**). These
116 faults are top-to-the-east, imbricated thrusts with a generally foreland-ward
117 propagation history in the Late-Cenozoic based on seismic- and field-based structural
118 analyses and low-temperature thermochronology (Hubbard & Shaw, 2009; Lu et al.,
119 2014; Tan et al., 2017). Crustal deformation has propagated into the Sichuan Basin,
120 culminating in the development of the Dayi fault, Xiongpo fault, Longquan Shan fault,
121 and associated fault-related folds (Jia et al., 2006; C. Sun et al., 2016). GPS
122 measurements show horizontal shortening rates are less than 3 mm/year across the
123 Longmen Shan thrust belt (Gan et al., 2007; G. Zheng et al., 2017).

124 Five major earthquakes took place during the past 1000 years (**Fig. 1**). The 1327
125 M 6 and 1941 M 6.2 Tianquan earthquake occurred near the southern end of the
126 Longmen Shan. The 1970 M_s 6.2 Dayi earthquake occurred in the current aftershock
127 gap. The 12 May, 2008 M_w 7.9 Wenchuan earthquake ruptured the surface in the
128 central and northern segments of the Longmen Shan along the BYF and
129 Jiangyou-Guanxian fault (e.g., Xu et al., 2009; Liu-Zeng et al., 2009). The 20 April,
130 2013 M_w 6.6 Lushan earthquake struck the south Longmen Shan. After the Lushan
131 earthquake, based on detailed field investigations, no surface rupture has been found;

132 only local compression ruptures were observed in concrete roads along the SDF (Xu
133 et al., 2013). According to the aftershock relocation, the 2008 Wenchuan earthquake
134 and the 2013 Lushan earthquake has a rupture length of ~300-350 km and ~35 km,
135 respectively (Huang et al., 2008; Y. Zheng et al., 2009; Fang et al., 2013, 2015). A gap
136 of ~50 km long is present in-between.

137

138 **3. Low-temperature Thermochronology**

139 **3.1. Previous Studies**

140 In the central and southern Longmen Shan, previous studies reported abundant
141 low-temperature thermochronology dates, as compiled in Fig. 2a. Arne et al. (1997)
142 and Kirby et al. (2002) reported the first low-temperature thermochronology evidence
143 of Late-Cenozoic rapid exhumation, with the method of fission track and (U-Th)/He,
144 respectively. Xu et al. (2000) and Wilson et al. (2011) reported fission track dates to
145 reveal Cenozoic incision histories in the plateau interior. Godard et al. (2009) showed
146 that the samples of Pengguan massif began to rapidly denudate at a rate of ~0.65
147 mm/yr since ~10 Ma according to (U-Th)/He dating and modeling. E. Wang et al.
148 (2012) systematically studied the low-temperature thermochronology of profile
149 samples in the Pengguan massif with elevation difference of ~3000 meters. They
150 obtained the Cenozoic cooling history of the Pengguan massif and discovered two
151 periods of rapid cooling events (30-25 Ma and 10-0 Ma). Tan et al. (2017) and Shen et
152 al. (2019) sampled the Xuelongbao massif in the hanging-wall of WMF, and unveiled

153 a rapid phase of denudation since 11-14 Ma with a rate of 0.8-1.2 mm/yr. Several
154 groups took detailed study in the Qingyi Jiang basin at the southern Longmen Shan,
155 and documented a rapid denudation history of rock masses on both sides of the
156 Wulong-Yanjing fault (WYF) since the Late Miocene (Tian et al., 2013; Cook et al.,
157 2013; Tan et al., 2014). Coincidentally or not, previous studies have mainly focused
158 on the Min Jiang and Qingyi Jiang drainage basins, largely overlapping the zones of
159 the 2008 Wenchuan and 2013 Lushan earthquake sequences, respectively.
160 Low-temperature thermochronology data is lacking within the aftershock gap,
161 inhibiting a systematic comparison of exhumation history along strike (**Fig. 2a**).

162

163 **3.2. Sampling Strategy, Method, and Results**

164 In order to constrain the Late-Cenozoic exhumation and faulting activities in the
165 aftershock gap of the Longmen Shan, we collected samples passing through the major
166 faults. To minimize the influence of elevation, all samples were collected in valley
167 bottoms. Because of the widespread limestone and mudstone in the study area, only
168 eight samples yielded sufficient apatite grains for AFT dating. Their locations are
169 listed in **Table 1** and plotted in **Fig. 2(a)**.

170 Sample preparation and experimental method followed T. Liu et al. (2001). Two
171 standard glass pieces, NBS SRM-612, calibrated against the fission-track age standard
172 Fish Canyon Tuff (Naeser et al., 1981), were wrapped tightly and irradiated with the
173 samples. Grain-by-grain and mica external detector techniques were adopted to obtain

174 individual grain ages (Wagner and Van den Haute, 2012). The Zeta value for the
175 standard glasses SRM-612 was 348.38 ± 20.7 (1σ) (Green, 1985; Hurford and Green,
176 1983).

177 **Fig. 3** and **Table 1** show the eight AFT ages and age spectra. AFT dating yield
178 two dates of ~ 6 Ma between the WYF and SDF (DY-01 and 04), and six dates
179 between ~ 18 and 44 Ma in the range front area between the SDF and Dayi fault
180 (DY-06, 07, 08, 12, 13, and 14). Three of the eight samples (i.e., DY-07, 08, and 14)
181 yield sufficient track length for thermal history modeling, as detailed below.

182

183 **3.3. Modeling and Interpretations on AFT Data**

184 Low-temperature thermochronology is a powerful approach to elucidate cooling
185 history of rock samples. In this study, we use the AFT method with closure
186 temperature ($110 \pm 10^\circ\text{C}$) (Brandon et al., 1998; Donelick et al., 2005). One advantage
187 of the AFT method is that the length distribution of fission tracks carries information
188 about the thermal history from closure temperature to surface temperature (e.g.,
189 Willett, 1997; Ketcham et al. 2007), especially for relative old samples.

190 Samples DY-01 and DY-04 located between the WYF and SDF yield young ages
191 of ~ 6 Ma. As they have very few spontaneous tracks, it is difficult to gather enough
192 track length for thermal history modeling. However, the young ages (~ 6 Ma) indicate
193 a rapid cooling rate ($\sim 15^\circ\text{C}/\text{Ma}$) from the closure temperature ($110 \pm 10^\circ\text{C}$) to the
194 ground surface temperature ($\sim 20^\circ\text{C}$) within ~ 6 Myr.

195 The other six samples located between the SDF and the Dayi fault show AFT

196 ages of ~20-44 Ma. Three of them (DY-07, 08, 14) resulted in sufficient (~100)
197 fission track length measurements. We used HeFTy tool to model their thermal
198 histories, based upon the annealing model by Ketcham et al. (2007). The modeling
199 results are shown in **Fig. 4**. All goodness of fit (GOFs) are greater than 0.9, indicating
200 high reliabilities (**Fig. 4**). We further utilized TERRA software (Ehlers, 2005) to
201 convert the cooling history to denudation history. The observed cooling history of
202 samples DY-07, 08, and 14 (all in the footwall of SDF) fit best with the denudation
203 rates between 0.3 and 0.4 mm/yr, while the cooling history of DY-01 and 04 from the
204 hanging-wall of SDF fit best with a denudation rate between 0.5 and 0.6 mm/yr (**Fig.**
205 **5**).

206

207 **4. Fluvial shear stress**

208 **4.1. Theoretical background**

209 Mechanical processes, including the rolling of bed load or suspended load,
210 weathering, and cavitation, cause bedrock incision. Channel river's gradient and
211 drainage area have a relationship with the rate of fluvial incision as a power function
212 (Howard, 1994):

$$213 \quad i = KA^mS^n \quad (1)$$

214 where i is incision rate, K is erodibility coefficient, A is drainage area, and S is river
215 gradient. Three physical variables, including stream power, unit stream power, and
216 fluvial shear stress, can lead to Eq. (1) (Howard et al., 1994; Slingerland et al., 1998).

217 While it is difficult to discriminate these variables' roles in incision, especially
218 between unit stream power and fluvial shear stress (Snyder et al., 2000), experiment
219 in the sub-Himalaya found that the fluvial shear stress correlates more consistently to
220 river incision rate than does the unit stream power (Lavé and Avouac, 2001).

221 The fluvial shear stress (τ) is defined as,

$$222 \quad \tau = \rho g R S \quad (2)$$

223 where ρ is water density, g is gravitational acceleration, R is hydraulic radius, and S is
224 stream slope. The hydraulic radius R is a function of channel width W and water depth
225 h (Lavé and Avouac, 2001)

$$226 \quad R = \frac{Wh}{W+2h} \quad (3)$$

227 The water depth can be expressed as a function of water discharge Q , channel width
228 W and depth-averaged velocity U (Manning's equation) (Chang, 1988),

$$229 \quad U = \frac{Q}{Wh} = \frac{1}{N} R^{2/3} S^{1/2} \quad (4)$$

230 where N is roughness coefficient ($N \propto D_{90}^{1/6}$, D_{90} is the grain diameter not exceeded
231 by 90% (in weight) of the bed load), and water discharge Q follows a power law
232 function of the drained area (Lavé and Avouac, 2001; Godard et al., 2010):

$$233 \quad Q = k \bar{P} A^{0.85} \quad (5)$$

234 According to Eq. (2) - (4), fluvial shear stress can be rewritten as (Godard et al.,
235 2010):

$$236 \quad \tau = \rho g \frac{(QN)^{3/5} S^{7/10}}{W^{3/5}} \quad (6)$$

237 Therefore, from Eq. (6), we can calculate the fluvial shear stress value after
238 obtaining these necessary parameters.

239

240 **4.2. Relative parameters calculations**

241 **4.2.1. Width (W)**

242 The bankfull width of the channels in the study area was mainly measured in the
243 field using distance-measuring equipment (product type Trupulse200B). For places
244 we cannot reach, we used SPOT 5m resolution panchromatic imagery to acquire the
245 bankfull width of the channel. We estimated a relative uncertainty of 5% exists on the
246 resulting width evaluation.

247 **4.2.2. Channel slope (S)**

248 The channel network was obtained from a 90 m DEM that is a blend of SRTM
249 (Jarvis et al., 2008). Each river was divided into ~20 segments, each of which has a
250 length of 2 - 4 km. We calculated the average channel slope of each segment, which is
251 equal to the altitude difference of the channel segment divided by the segment length
252 along the channel. We assume a relative uncertainty of 10% on the slope calculations.

253 **4.2.3. Discharge (Q)**

254 We acquired 10-year return discharge (Q_{10}) from two monitoring stations (Qin,
255 2006). The maximum discharge of the Duoyinping station, located on the Qingyi
256 Jiang, was ~1000 m³/s; the maximum discharge of the Xuankou station on the main
257 channel of Min Jiang was ~1000 m³/s (Qin, 2006). We assumed that the spatial

258 variations of precipitation rate are relatively limited over the drainage basin. We
259 related Q_{10} to area A as $Q \propto A^{0.85}$ (Lavé and Avouac, 2001), and acquired the
260 discharge for each survey point along the Qingyi Jiang, Yuxi He, and Shaotang He
261 rivers. For the Q_{10} along the Chu He and Xi He rivers, we assumed that the
262 precipitation rates were similar between the drainage basins of the Qingyi Jiang and
263 Yuxi He rivers. An estimated relative uncertainty of 25% exists on the 10-year return
264 discharge calculations.

265 **4.2.4. Sediments size and roughness coefficient (N)**

266 Incising channels in actively-deforming orogenic belts have a large alluvial cover
267 and size distribution of bed sediment. Not only can sediments provide working tools
268 for abrasion to cause bedrock incision, but they also have protection for bedrock
269 (Sklar and Dietrich, 2004). Grain size and sediments supply are fundamental controls
270 on bedrock incision rates (Sklar and Dietrich, 2004). D_{90} is required in fluvial shear
271 stress calculation. We performed bedload counting on photos taken by UAV on
272 typical areas for each surveyed river, and estimated D_{90} for each river. For the
273 roughness coefficient N , we first chose a value of 0.1 for the Shaotang He, to make
274 the fluvial shear stress values in the Pengguan massif similar between the Shaotang
275 He and Min Jiang (Godard et al., 2010). Then we derived the roughness coefficient
276 for other four rivers according to $N \propto D_{90}^{1/6}$ (Chang, 1988; Lavé and Avouac, 2001).
277 The values of D_{90} and N for each river are shown in **Table S1**.

278

279 **4.3. Individual fluvial shear stress profiles**

280 Fluvial shear stress values of the Qingyi Jiang, Yuxi He, Chu He, Xi He, and
281 Shaotang He rivers are calculated from Eq. (6) along the surveyed streams where
282 relevant parameters were measured (**Figs. 2 & 6**).

283 The Qingyi Jiang flows through the Proterozoic Baoxing massif, crosses the
284 WYF and flows on the Mesozoic sedimentary units in its lower reach. The fluvial
285 shear stress of the Qingyi Jiang changes markedly across the WYF. The average value
286 in the hanging-wall block of WYF is ~890 Pa; in the footwall, it is ~480 Pa (**Fig. 6a**).

287 Northward, the Yuxi He is a major tributary of the Qingyi Jiang river basin in the
288 southern Longmen Shan. It crosses the entire Baoxing massif that is bound by the
289 WYF and the SDF, and flows into Mesozoic sedimentary rocks at the range front. The
290 values of fluvial shear stress are somewhat complicated because of both the lithology
291 change and the fault activity. Overall, the river poses greater fluvial shear stress to the
292 hanging-wall of the SDF than its footwall (**Fig. 6b**).

293 Further north, the Chu He is the main river of a small range frontal catchment
294 drainage. It follows, for several kilometers, along the SDF. With similar lithology on
295 both sides along the SDF, the fluvial shear stress value drops significantly along the
296 SDF, indicating highly fractured rocks caused by fault activity. The average fluvial
297 shear stress value in the hanging-wall and footwall blocks of the SDF are ~ 170 Pa
298 and ~100 Pa, respectively, while it is ~50 Pa along the fault (**Fig. 6c**).

299 The Xi He presents similar lithologic features to the Chu He. Bedrocks along the
300 river are mainly sandstones and limestones. Although the fluvial shear stress does not

301 change significantly across the SDF, its value in the hanging-wall block of SDF (~280
302 Pa) is almost twice that of the footwall block (~150 Pa) (**Fig. 6d**).

303 The Shaotang He is a major tributary of the Min Jiang. It flows from south to
304 north in the Paleozoic-Triassic rocks, crosses the WMF, flows into the Proterozoic
305 Pengguan massif, and merges into the Min Jiang near the BYF. The average fluvial
306 shear stress in the footwall block of WMF (~ 450 Pa) is higher than that in the
307 hanging-wall (~ 260 Pa), which may be due to lithological contrast: the footwall block
308 mainly contains granitoids whereas the hanging-wall block is covered largely by
309 sandstones (**Fig. 6e**).

310

311 **4.4. Calibration between fluvial shear stress values and erosion rate**

312 A nondimensional parameter termed Shields stress (τ^*) is an indicator for
313 riverbed mobility, based on reach and cross-sectional average properties ([Parker,](#)
314 [1978](#)). It is given by

$$315 \tau^* = \frac{hS}{(\rho_s/\rho - 1) D_{50}} \quad (7)$$

316 where ρ_s and ρ are density of gravel and water, respectively, D_{50} is the grain
317 diameter not exceeded by 50% (in weight) of the bed load ([Lavé and Avouac, 2001](#)).

318 Based on Eqs. (2), (3) and (7), the Shields stress can be written to

$$319 \tau^* = \frac{\tau}{(\rho_s - \rho) g D_{50}} \quad (8)$$

320 The Shields stress, when exceeds a threshold value, yield a more consistent
321 relationship with the fluvial incision rate than the fluvial shear stress ([Lavé and](#)

322 [Avouac, 2001](#)). For same or similar lithology (under similar abrasion), the Shields
323 stress and incision rate (i) have a positive linear correlation ([Lavé and Avouac, 2001](#)):

$$324 \quad i = K(\tau^* - \tau_c^*) \quad (9)$$

325 where K is erodibility coefficient, mainly related to lithological properties of the
326 bedrock, τ_c^* is the critical Shields stress value for incipient motion. The range of the
327 critical Shields stress is 0.03 to 0.08, depending on shear velocity, D_{50} , and kinematic
328 viscosity of fluid ([Neill, 1968](#); [Buffington and Montgomery, 1997](#)).

329 In this study, a uniform value of D_{50} was selected, because of the similar scale of
330 the rivers and nearly identical tectonic and climatic background. Therefore, a linear
331 relationship between the Shields stress and fluvial shear stress emerges on the basis of
332 Eq. (8), and a positive linear correlation between the fluvial shear stress value and
333 erosion rate is expected. Upon finding this correlation, one can acquire the erosion
334 rates for all survey points ([Lavé and Avouac, 2001](#); [Godard et al., 2010](#)). The fluvial
335 shear stress at the segment flowing out of the mountain is usually 1.4 times of the
336 critical value ([Paola and Mohrig, 1996](#); [Lavé and Avouac, 2001](#)). We calculated the
337 average fluvial shear stress along the first kilometers downstream of the outlet of the
338 Chu He, Xi He, and Qingyi Jiang rivers, and obtained an average critical fluvial shear
339 stress of ~50 Pa. Then according to Eq. (8) with the critical Shields stress of 0.03-0.08,
340 we derived that D_{50} is 4-10 cm, which is comparable to the D_{50} value (8 cm) estimated
341 by [Godard et al. \(2010\)](#).

342 We divided the rocks into two groups, granitoid and sedimentary rocks,
343 according to the distinct abrasion rate of rocks in the study area ([Godard et al., 2010](#)).

344 Then, we established a linear relationship between the fluvial shear stress value and
345 erosion rate for each rock type (**Fig. 7**). Using average erosion rates from
346 low-temperature thermochronology data, we performed an empirical calibration of the
347 erodibility coefficient in Eq. (9). The denudation rates are equal to the erosion rates in
348 the study area, because no portion of denudation resulted from extensional tectonics
349 here.

350 For river segments in the granitoid rocks, in the hanging-wall of the WYF along
351 the Qingyi Jiang, the average fluvial shear stress is ~ 800 Pa, and the erosion rate is
352 1-1.5 mm/yr. In the footwall of the WYF along the same river, the values are ~ 460 Pa
353 and 0.7-0.8 mm/yr, respectively. In the footwall of WMF along the Shaotang He river,
354 ~ 450 Pa and 0.6-0.7 mm/yr, respectively.

355 For river segments in sedimentary rocks, in the hanging-wall of WMF along the
356 Shaotang He, the average fluvial shear stress is ~ 260 Pa and the erosion rate is 0.7-0.8
357 mm/yr. In the hanging-wall of the SDF along both the Xi He and the Chu He rivers,
358 ~ 250 Pa and 0.5-0.6 mm/yr, respectively. The average fluvial shear stress value in the
359 footwall of the SDF along the Xi He and Chu He is ~ 150 Pa and ~ 120 Pa,
360 respectively, and the erosion rate is 0.3-0.4 mm/yr for both river segments (**Fig. 7**).

361 We computed weighted regression lines that go through each set of data and the
362 critical fluvial shear stress. The latter has value of ~ 50 Pa at a zero incision rate and
363 corresponds to the pebble threshold motion ([Lavé and Avouac, 2001](#)). Data from the
364 sedimentary rocks and the Precambrian granitoid basement display distinct trends
365 with a slope of 0.0035 and 0.0017, respectively (**Fig. 7**). The newly obtained

366 empirical erodibility coefficients allowed us to calculate the erosion rates for each
367 survey point on fluvial shear stress, as discussed in section 5.2 below.

368

369 **5. Discussion**

370 **5.1. Reliability of the empirical relationship**

371 The erosion rates obtained in this study show good linear relationship with the
372 fluvial shear stress values in both the granitoid rocks and sedimentary rocks, with $R^2 >$
373 0.9. The 2-fold difference between the regression slopes of two rock families are
374 similar to those of Godard et al. (2010), although the slopes (0.0017 and 0.0035) in
375 this study are ~40% higher than those in Godard et al. (2010) (0.0012 and 0.0024,
376 respectively).

377 We used the denudation rates derived from thermochronology dates only, while
378 Godard et al. (2010) use those from both thermochronology and cosmogenic dates,
379 mainly the later one. Godard et al. (2010) noted that their ^{10}Be -derived erosion rates
380 may be lower than the actual long-term values because their rates (in a time period of
381 ~1.5 ka) may not include the contribution of great earthquakes due to their relative
382 long recurrence intervals (~3 ka) (Ran et al., 2010). Therefore, we suggest that the
383 regression slopes between erosion rate and fluvial shear stress value in this study are
384 more representative for the long-term average erosion in the central and southern
385 Longmen Shan.

386 Moreover, when the regression slopes of **Fig. 7** are converted to equivalent

387 erodibility by multiplying a factor of ~ 1667 (the critical fluvial shear stress of 50 Pa
388 corresponding to the Shields stress of 0.03, and $50/0.03 \approx 1667$), the erodibility
389 coefficients of the granitoids and sedimentary rocks in this study are ~ 2.8 and ~ 5.8
390 mm/yr, respectively. They are comparable with the erodibility values (~ 2 and ~ 7
391 mm/yr) converted from the abrasion values by flume experiments (Godard et al.,
392 2010).

393 In summary, the high R^2 (> 0.9) and the similarity of the erodibility coefficient
394 between the two independent approaches enhance the reliability of the empirical
395 linear relationship between the fluvial shear stress value and erosion rate in this study.

396

397 **5.2. Spatial pattern of erosion and its implications**

398 *5.2.1 Erosion and deformation across the aftershock gap*

399 The new fission track data in this study allow us to document the erosion
400 difference across the range in the aftershock gap, and evaluate the relationship
401 between surface erosion and deep structure. We plotted AFT ages and their
402 corresponding erosion rates in a profile X-X' across the aftershock gap (**Fig. 8**). Five
403 domains of erosion rate exist from the Siguniang pluton in the hinterland to the
404 Sichuan Basin (**Fig. 8**). In the hinterland far from the thrusts, the erosion rate is
405 between 0.1 and 0.5 mm/yr. Approaching the thrust belt, it increases to ~ 0.7 mm/yr.
406 This is probably an underestimate, as the only AFT age in this domain (~ 4.9 Ma,
407 Wilson et al., 2011) was ca. 20 km from the WYF (**Fig. 2a**). The erosion rate drops

408 stepwise to 0.5-0.6 mm/yr, then 0.3-0.4 mm/yr, and then zero across the WYF, SDF,
409 and Dayi fault, respectively.

410 We built a crustal-scale section below profile X-X' (**Fig. 8**). All major faults in
411 the X-X' section show reverse faulting, consistent with those to the north and south
412 (Tian et al., 2013; Tan et al., 2014, 2017; Shen et al., 2019). For structures in the
413 shallow crust at the mountain front, we largely adopted the seismic interpretations by
414 Z. Li et al. (2017) on the geometry of the Dayi fault, the Range Front blind thrust
415 (RFBT), and the shallow detachment fault localized in the Triassic in the Sichuan
416 Basin. The hypocenter of the 1970 Dayi earthquake constrained the RFBT geometry
417 down to ~ 14 km. We inferred that the major thrusts (WYF, SDF, and RFBT) have a
418 listric geometry and sole into a sub-horizontal detachment fault/ductile shear zone at
419 ca. 20 km (Hubbard and Shaw, 2009; Tan et al., 2019). Underlying the detachment is
420 a zone of partially molten mid-crust that must have displayed out-of-plane motions
421 (possibly with a dextral sense-of-motion), as inferred from the low-velocity anomalies
422 and orogen-parallel azimuthal anisotropy (e.g., Z. Liu et al., 2018; Bao et al., 2020).
423 We also speculated reverse faulting in the lower crust and across the Moho
424 discontinuity, as detected in the north-central Longmen Shan (Guo et al., 2013; Feng
425 et al., 2016). Depth of the Moho varies from ~58 km under the eastern Tibetan Plateau
426 to ~42 km under the Sichuan Basin, displaying a “Moho ramp” under the southern
427 Longmen Shan (Lu et al., 2019; Tan et al., 2019). The maximum erosion rate in this
428 segment (the aftershock gap) of the Longmen Shan is located in the hanging-wall of
429 WYF (**Fig. 8**), consistent with the “Maximum exhumation belt” along the eastern

430 Tibetan Plateau margin proposed by Tan et al. (2019).

431

432 *5.2.2 Along-strike variations in erosion*

433 Below we focus on the spatial variations of erosion between the aftershock gap
434 and surrounding areas. We plotted the erosion rates derived from two independent
435 methods, i.e., low-temperature thermochronology and fluvial shear stress analyses, on
436 the map (for the latter dataset) and in five profiles (for both datasets) (**Fig. 9**).

437 The thermochronology-derived erosion rates agree well with those derived from
438 fluvial shear stress analysis (**Fig. 9b**). In profile A-A', previous thermochronological
439 studies have revealed an average erosion rate of 0.8-1.2 mm/yr in the hinterland,
440 0.6-0.7 mm/yr in the hanging-wall block of the BYF, and ~0.2 mm/yr or less at the
441 range front (Godard et al., 2009; Tan et al., 2017; Shen et al., 2019). Profile C-C'
442 shows a similar trend of decreasing erosion rate in different fault blocks: 1.0-1.4
443 mm/yr in the hanging-wall block of the WYF, 0.7-0.8 mm/yr in its footwall, and less
444 than 0.2 mm/yr at the range front (Arne et al., 1997; Tian et al., 2013; Cook et al.,
445 2013; Tan et al., 2014). The erosion rates obtained by fluvial shear stress are only
446 available for the footwall block of WMF in profile A-A' and the footwall block of
447 WYF in profile C-C'. Their values (0.70 ± 0.25 mm/yr and 0.70 ± 0.24 mm/yr,
448 respectively) are consistent with those obtained by low-temperature
449 thermochronology.

450 On profile B-B', the AFT age (~4.9 Ma) in the hanging-wall of WYF (Wilson et
451 al., 2011) corresponds to an erosion rate of ~0.7 mm/yr (**Fig. 9b**). This is comparable

452 with the erosion rate of 0.74 ± 0.44 mm/yr calculated from fluvial shear stress. In the
453 footwall block of WYF, the erosion rate obtained from the two AFT ages by this study
454 is 0.5-0.6 mm/yr (**Fig. 5**) and the erosion rate inferred from fluvial shear stress is 0.70
455 ± 0.31 mm/yr. The AFT-derived erosion rate in the footwall of SDF is 0.3-0.4 mm/yr
456 (**Fig. 5**), largely agreeing with the 0.28 ± 0.15 mm/yr erosion rate obtained from
457 fluvial shear stress analysis. The erosion rate of 0.3-0.4 mm/yr at the range front of
458 the gap is comparable with the slip rate calculated from seismic reflection profiles ([Z.
459 Li et al., 2017](#)).

460 Such a consistency in all three profiles supports previous argument ([Liu-Zeng et
461 al., 2011](#); [Z. Li et al., 2016](#); [Y. Liu et al., in review](#)) that the central and southern
462 Longmen Shan has reached a steady-state since the Pliocene.

463 We further plotted two orogen-parallel profiles D-D' and E-E' to portray the
464 along-strike variations in erosion rate between the aftershock gap and adjacent areas
465 (**Fig. 9c**). In the hinterland profile D-D', while elevation is generally higher in the
466 aftershock gap than the adjacent areas, the erosion rate is lower in the gap (**Fig. 9c**).
467 On the contrary, in the range frontal profile E-E', both elevation and erosion rate are
468 greater in the gap. This along-strike variation indicates that the frontal range of the
469 gap undergoes more rapid erosion, and implies that fault activities within the gap are
470 more localized at the mountain front, in comparison with the adjacent areas. This
471 inference is further supported by the latest fault activity based on the deformation of
472 young strata, and the fact that the 1970 M_s 6.2 Dayi earthquake occurred under the
473 range front of the gap (**Figs. 1, 8, & 9a**) ([Densmore et al., 2007](#); [H. Wang et al., 2013](#);

474 [Dong et al., 2017; Shao et al., 2019](#)). If true, this lateral variation in fault activity may
475 be related to the sudden stop of seismic ruptures and distribution of aftershocks in the
476 2008 Wenchuan and 2013 Lushan earthquakes.

477

478 **5.3. Mechanism for the aftershock gap: weak material vs.** 479 **differential erosion**

480 In this section, we evaluate the existing mechanism (weak material) ([Z. W. Li et](#)
481 [al., 2013; Pei et al., 2014; Liang et al., 2018](#)) and the alternative hypothesis
482 (differential erosion) for the formation of the aftershock gap. Given that the central
483 and southern Longmen Shan thrust belt has reached a steady-state over the past a few
484 Myr ([Liu-Zeng et al., 2011; Z. Li et al., 2016](#)), the two models would produce distinct
485 pattern of erosion, which can be tested against aforementioned observations.

486 Here we use the critical-taper wedge theory to characterize the deformation and
487 earth surface processes in the Longmen Shan thrust belt ([Hubbard et al., 2010](#)). The
488 critical-taper wedge theory ([Davis et al., 1983; Suppe, 2007](#)) depicts an elegant
489 relationship between the geometry and mechanics of a subaerial, critically-tapered
490 thrust wedge:

$$491 \alpha + \beta = \frac{\beta + F}{1 + W} \quad (9)$$

492 where α is surface slope; β , detachment dip; F , detachment fault strength; and W ,
493 wedge strength.

494 We follow Y. Liu et al. ([in review](#)) to build conceptual wedge models to assess

495 the competing hypotheses. Consider a three-dimensional, critically-tapered thrust
496 wedge that undergoes uniform shortening, and the central portion represents the
497 aftershock gap. In the “weak material” model, as the wedge strength (W) decreases
498 (due to the presence of mechanically weaker materials) while other variables (i.e.,
499 detachment dip, detachment depth, detachment fault strength, and shortening strain)
500 remain unchanged, according to Eq. (9), the surface slope (α) should increase to attain
501 a new, greater taper. The hinterland of the recess (where the wedge strength is reduced)
502 witnesses greater tectonic uplift than do the portions on both sides. In contrast, the
503 frontal part of the wedge at the recess experiences a smaller amount of tectonic uplift
504 than do the adjacent portions. Thereby, along-strike variations in uplift emerge. As the
505 propagation of the deformation front stalls, a recess structure appears (**Fig. 10a**). In a
506 critically-tapered wedge, this results in higher elevation and greater erosion rate at the
507 recess along the hinterland profile F-F’ (**Fig. 10b**). In the meantime, it produces lower
508 elevation and smaller erosion rate at the recess along the range-frontal profile G-G’
509 (**Fig. 10c**).

510 We conduct another “conceptual experiment” on a three-dimensional,
511 critically-tapered thrust wedge for the “differential erosion” model. It also undergoes
512 uniform shortening (**Fig. 10d**). If erosion (\mathcal{E}) is reduced in the central portion while
513 other variables remain unchanged along strike, after reaching a new steady-state, the
514 wedge attains the same critical taper everywhere, because the intrinsic properties of
515 the wedge are identical everywhere in this model (Marshak, 2004; Y. Liu et al., in
516 [review](#)). Consequently, the central portion of the wedge is more readily to propagate

517 foreland-ward whereas the adjacent portions are prone to stall. A salient forms (**Fig.**
518 **10d**). The surface slope across the salient should be identical with that of the adjacent
519 portions. Hinterland of the salient is expected to gain a higher elevation and display a
520 smaller erosion rate, due to the reduced erosion in this scenario. A cartoon profile H-H'
521 demonstrates such along-strike variations in the hinterland (**Fig. 10e**). At the range
522 front, both elevation and erosion rate at the salient should be slightly greater than
523 those of the adjacent portions, as shown in the cartoon profile J-J' (**Fig. 10f**).

524 The “weak material” model can be represented by the first conceptual
525 experiment (**Fig. 10a**), whereas the “differential erosion” hypothesis corresponds to
526 the latter one (**Fig. 10d**). Based on the results in previous section, the topography and
527 erosion rate patterns predicted by the first model are at odds with the observed
528 patterns at the aftershock gap (**Fig. 10b&c** vs. **Fig. 9c**). On the contrary, predictions of
529 the second model agree well with the observations of topography and erosion rates
530 around the aftershock gap (**Fig. 10e&f** vs. **Fig. 9c**). These comparisons indicate that
531 along-strike variation in erosion could be the main cause for the formation of the
532 aftershock gap and fault segmentation. In other words, due to the heterogeneous,
533 weaker erosion in the hinterland of the gap, deformation in the Longmen Shan thrust
534 wedge propagated to the Sichuan Basin more favorably than its adjacent portions,
535 resulting in the lateral difference of fault activity.

536 The Longmen Shan provides an ideal natural archive to study the erosional
537 influence on tectonics through lateral comparison, thanks to the steep topography,
538 active tectonics, and large rivers that cut through the Longmen Shan. Previous studies

539 (Tan et al., 2018; Y. Liu et al., in review) and this study show that erosion has indeed
540 exerted an important influence on the fault segmentation in the Longmen Shan thrust
541 belt. If all conditions except erosion are uniform in a critically-tapered orogenic
542 wedge, recess emerges in the region with strong erosion (Marshak, 2004). The
543 Dujiangyan recess in the central Longmen Shan is proposed to be such a recess
544 controlled by lateral differential erosion (Y. Liu et al., in review). This mechanism on
545 the surface also affected the coseismic slip during the 2008 Wenchuan earthquake
546 (Tan et al., 2018). Therefore, in an orogenic belt with strong erosion such as the
547 Longmen Shan, along-strike variations in structural geometry, although sometimes
548 used as a mark for multi-stage deformation, could be simply controlled by the lateral
549 difference of erosion. One shall not ignore the erosional impact.

550

551 **5.4. Implication for seismicity: Asperity model vs. Barrier model**

552 Paleoseismology studies suggest that earthquakes recurrent on a given fault may
553 often have characteristic length and amount of slip (e.g., Wallace, 1981; Sieh, 1981;
554 Wesnousky et al., 1982). Asperity model and barrier model have been raised up to
555 explain this phenomenon (Aki, 1984). Both terms, “asperity” and “barrier”, refer to
556 strong patches on fault surfaces that resist breaking. However, the roles of strong
557 patches in the rupture process are distinctly different (Fig. 11a&b) (Aki, 1984). In the
558 asperity model, the fault plane contains a strong patch surrounded by a slip-released
559 region before an earthquake, and stress becomes homogeneous after an earthquake

560 (Fig. 11a). In the barrier model, the fault plane is uniformly stressed before an
561 earthquake, and it contains unbroken strong patches in postseismic stage (Fig. 11b).

562 The competing hypotheses for the aftershock gap in Longmen Shan correspond
563 to the two theoretical models. The weak material hypothesis argues that the fault
564 plane in the gap undergoes ductile deformation and are hardly stressed, which
565 matches the asperity model (Fig. 11a). The differential erosion hypothesis, on the
566 other hand, mimics the barrier model (Fig. 11b). It considers the fault block between
567 the BYF and WYF as a stress barrier, because of the high topography within the gap.
568 Shortening across the gap are accommodated by the thrust faults in the foreland
569 region (Fig. 11c). According to the aforementioned analyses, the barrier model may
570 better explain the characteristic earthquake appearance in the Longmen Shan (e.g.,
571 [Ran et al., 2010](#)). The active faults at the range front area within the gap, therefore,
572 imposes high seismic risks to the region. This is remarkably different from the seismic
573 assessment based on the asperity model. Our inference agrees with Z. Li et al. (2017),
574 who alerted the potential of great earthquakes at the range front of the southern
575 Longmen Shan. While trenches on the SDF within the aftershock gap had revealed
576 several paleo-earthquakes over the past 3000 years, which may have reduced the
577 recent earthquake risk on this fault ([H. Wang et al., 2015](#); [Dong et al., 2017](#); [Shao et](#)
578 [al., 2019](#)), the potential risk on other active faults should not be overlooked.

579

580 **6. Conclusions**

581 We have proposed an alternative explanation for the aftershock gap in the

582 southern Longmen Shan, eastern Tibetan Plateau margin: differential erosion induced
583 along-strike variations in fault activity. To testify the new explanation and pre-exist
584 explanation (weak material), we have studied the spatial distribution of erosion at the
585 aftershock gap of the Longmen Shan, based on low-temperature thermochronology
586 and fluvial shear stress analysis. We draw the following conclusions:

587 (1) We have reported eight apatite fission track dates within the aftershock gap: ~6-44
588 Ma. Our modeling revealed that the erosion rate of the fault block between WYF
589 and SDF is 0.5-0.6 mm/yr, while the footwall of the SDF is 0.3-0.4 mm/yr, since
590 ~8 Ma.

591 (2) We have calculated the erosion rate for ~800 survey points of fluvial shear stress
592 along five rivers around the aftershock gap, based on the empirical relationship
593 between the fluvial shear stress and erosion rate.

594 (3) Along-strike variations in erosion rate and topography exist in the aftershock gap.
595 In the hinterland, while elevation is generally higher in the gap than the adjacent
596 areas, the erosion rate is lower in the gap. Along the range front, both elevation
597 and erosion rate are greater in the gap.

598 (4) We have built two conceptual critical-taper wedge models to evaluate the “weak
599 material” and “differential erosion” hypotheses. Comparison between model
600 predictions and our observations strongly favors the differential erosion as the
601 main cause for the aftershock gap and fault segmentation.

602 (5) This study implies that the aftershock gap in the southern Longmen Shan is not a
603 ductile deformation zone, but a barrier for the rupture during the 2008 Wenchuan

604 earthquake, which needs serious consideration for seismic risk assessment.

605

606 **Acknowledgments**

607 This study is supported by the Integrated Study on Seismotectonic Models for
608 Typical Regions of China Earthquake Administration (grant number F-18-04), and the
609 GURI Fund from the State of Texas and the University of Houston. We thank Fang
610 Xu for her help in fieldwork. The topography data (SRTM data V4) is from the
611 website (<http://srtm.csi.cgiar.org>). The data of aftershock of the 2008 Wenchuan
612 earthquake is from Huang et al. (2008). The data of aftershock of the 2013 Lushan
613 earthquake is from Fang et al. (2013). The rock abrasion data are from Godard et al.
614 (2010). The data in Tables S1 is publicly available
615 (<https://doi.org/10.5281/zenodo.3739423>).

616

617

618 **References**

- 619 Arne, D., Worley, B., Wilson, C., Chen, S. F., & Dirks, P. (1997). Differential
620 exhumation in response to episodic thrusting along the eastern margin of the
621 tibetan plateau. *Tectonophysics*, 280(3-4), 239-256.
- 622 Arrowsmith, J. R., & Strecker, M. R. (1999). Seismotectonic range-front
623 segmentation and mountain-belt growth in the Pamir-Alai region, Kyrgyzstan
624 (India-Eurasia collision zone). *Geological Society of America Bulletin*, 111(11),
625 1665-1683.
- 626 Avouac, J. P., & Burov, E. B. (1996). Erosion as a driving mechanism of
627 intracontinental mountain growth. *Journal of Geophysical Research: Solid Earth*,
628 101(B8).

629 Bao, X., Song, X., Eaton, D. W., Xu, Y., & Chen, H. (2020). Episodic lithospheric
630 deformation in eastern Tibet inferred from seismic anisotropy. *Geophysical*
631 *Research Letters*, 47(3), e2019GL085721.

632 Brandon, M. T., Roden-Tice, M. K., & Garver, J. I. (1998). Late Cenozoic exhumation
633 of the Cascadia accretionary wedge in the Olympic Mountains, northwest
634 Washington State. *Geological Society of America Bulletin*, 110(8), 985-1009.

635 Burchfiel, B. C., Zhiliang, C., Yupinc, L., & Royden, L. H. (1995). Tectonics of the
636 Longmen Shan and adjacent regions, central China. *International Geology*
637 *Review*, 37(8), 661-735.

638 Buffington, J. M., & Montgomery, D. R. (1997). A systematic analysis of eight
639 decades of incipient motion studies, with special reference to gravel-bedded
640 rivers. *Water Resources Research*, 33(8), 1993-2029.

641 Burchfiel, B. C., Zhiliang, C., Yupinc, L., & Royden, L. H. (1995). Tectonics of the
642 Longmen Shan and adjacent regions, Central China. *International Geology*
643 *Review*, 37(8), pp.661-735.

644 Chang, H. H. (1988). *Fluvial processes in river engineering*: Malabar, Fla.

645 Chen, S. F., Wilson, C. J. L., Deng, Q. D., Zhao, X. L., & Zhi, L. L. (1994). Active
646 faulting and block movement associated with large earthquakes in the Min Shan
647 and Longmen Mountains, northeastern Tibetan Plateau. *Journal of Geophysical*
648 *Research: Solid Earth*, 99(B12), 24025-24038.

649 Clark, M. K., & Royden, L. H. (2000). Topographic ooze: Building the eastern margin
650 of Tibet by lower crustal flow. *Geology*, 28(8), 703-706.

651 Calais, E., Freed, A. M., Arsdale, R. V., & Stein, S. (2010). Triggering of new Madrid
652 seismicity by late-pleistocene erosion. *Nature*, 466(7306), P.608-611.

653 Cook, K. L., Royden, L. H., Burchfiel, B. C., Lee, Y. H., & Tan, X. (2013).
654 Constraints on Cenozoic tectonics in the southwestern Longmen Shan from
655 low-temperature thermochronology. *Lithosphere*, 5(4), 393-406.

656 Davis, D., Suppe, J., & Dahlen, F. A. (1983). Mechanics of fold-and-thrust belts and
657 accretionary wedges. *Journal of Geophysical Research: Solid Earth*, 88(B2),
658 1153-1172.

659 Densmore, A. L., Ellis, M. A., Li, Y., Zhou, R., Hancock, G. S., & Richardson, N.
660 (2007). Active tectonics of the Beichuan and Pengguan faults at the eastern
661 margin of the Tibetan Plateau. *Tectonics*, 26(4).

662 de Sigoyer, J., Vanderhaeghe, O., Duchêne, S., & Billerot, A. (2014). Generation and
663 emplacement of Triassic granitoids within the Songpan Ganze
664 accretionary-orogenic wedge in a context of slab retreat accommodated by tear
665 faulting, Eastern Tibetan plateau, China. *Journal of Asian Earth Sciences*, 88,
666 192-216.

667 Donelick, R. A., O'Sullivan, P. B., & Ketcham, R. A. (2005). Apatite fission-track

668 dating. *Reviews in Mineralogy & Geochemistry*, 527-565.

669 Dong, S. P., Han, Z. J., & An, Y. F. (2017). Paleoseismological events in the “seismic
670 gap” between the 2008 Wenchuan and the 2013 Lushan earthquakes and
671 implications for future seismic potential. *Journal of Asian Earth Sciences*, 135,
672 1-15.

673 Ehlers, T. A. (2005). Crustal thermal processes and the interpretation of
674 thermochronometer data. *Reviews in Mineralogy and Geochemistry*, 58(1),
675 315-350.

676 Fang, L., Wu, J., Wang, W., Du, W., Su, J., Wang, C., ... & Cai, Y. (2015). Aftershock
677 observation and analysis of the 2013 Ms7.0 Lushan earthquake. *Seismological
678 Research Letters*, 86(4), 1135-1142.

679 Fang, L., Jianping, W. U., Weilai, W., Zuoyong, L., Changzai, W., & Ting, Y., et al.
680 (2013). Relocation of the mainshock and aftershock sequences of Ms7.0 Sichuan
681 Lushan earthquake. *Chinese Science Bulletin*, 058(028), 3451-3459.

682 Gan, W., Zhang, P., Shen, Z. K., Niu, Z., Wang, M., Wan, Y., ... & Cheng, J. (2007).
683 Present-day crustal motion within the Tibetan Plateau inferred from GPS
684 measurements. *Journal of Geophysical Research: Solid Earth*, 112(B8).

685 Godard, V., Pik, R., Lavé, J., Cattin, R., Tibari, B., De Sigoyer, J., ... & Zhu, J. (2009).
686 Late Cenozoic evolution of the central Longmen Shan, eastern Tibet: insight
687 from (U-Th)/He thermochronometry. *Tectonics*, 28(5).

688 Godard, V., Lavé, J., Carcaillet, J., Cattin, R., Bourlès, D., & Zhu, J. (2010). Spatial
689 distribution of denudation in Eastern Tibet and regressive erosion of plateau
690 margins. *Tectonophysics*, 491(1-4), 253-274.

691 Green, P. F. (1985). Comparison of zeta calibration baselines for fission-track dating
692 of apatite, zircon and sphene. *Chemical Geology: Isotope Geoscience section*,
693 58(1-2), 1-22.

694 Horton, B. K. (1999). Erosional control on the geometry and kinematics of thrust belt
695 development in the central Andes. *Tectonics*, 18(6), 1292-1304.

696 Huang, Y., Wu, J., Zhang, T., & Zhang, D. (2008). Relocation of the M8.0 Wenchuan
697 earthquake and its aftershock sequence. *Science in China Series D: Earth
698 Sciences*, 51(12), 1703-1711.

699 Hubbard, J., & Shaw, J. H. (2009). Uplift of the Longmen Shan and Tibetan plateau,
700 and the 2008 Wenchuan (M= 7.9) earthquake. *Nature*, 458(7235), 194-197.

701 Hubbard, J., Shaw, J. H., & Klinger, Y. (2010). Structural Setting of the 2008 Mw 7.9
702 Wenchuan, China, Earthquake. *Bulletin of the Seismological Society of America*, 100(5B),
703 2713-2735.

704
705 Hurford, A. J., & Green, P. F. (1983). The zeta age calibration of fission-track dating.
706 *Chemical Geology*, 41, 285-317.

707 Jarvis, A., Reuter, H. I., Nelson, A., & Guevara, E. (2008). Hole-filled SRTM for the
708 globe Version 4. *available from the CGIAR-CSI SRTM 90m Database*
709 (<http://srtm.csi.cgiar.org>), 15, 25-54.

710 Jia, D., Wei, G., Chen, Z., Li, B., Zeng, Q., & Yang, G. (2006). Longmen Shan
711 fold-thrust belt and its relation to the western Sichuan Basin in central China:
712 New insights from hydrocarbon exploration. *AAPG Bulletin*, 90(9), 1425-1447.

713 Jin, W., Tang, L., Yang, K., Wan, G., & Lü, Z. (2010). Segmentation of the Longmen
714 Mountains thrust belt, western Sichuan foreland basin, SW China.
715 *Tectonophysics*, 485(1-4), 107-121.

716 Ketcham, R. A., Carter, A., Donelick, R. A., Barbarand, J., & Hurford, A. J. (2007).
717 Improved measurement of fission-track annealing in apatite using c-axis
718 projection. *American Mineralogist*, 92(5-6), 789-798.

719 Kirby, E., Reiners, P. W., Krol, M. A., Whipple, K. X., Hodges, K. V., Farley, K. A., ...
720 & Chen, Z. (2002). Late Cenozoic evolution of the eastern margin of the Tibetan
721 Plateau: Inferences from $^{40}\text{Ar}/^{39}\text{Ar}$ and (U-Th)/He thermochronology. *Tectonics*,
722 21(1), 1-1.

723 Lavé, J., & Avouac, J. P. (2001). Fluvial incision and tectonic uplift across the
724 Himalayas of central Nepal. *Journal of Geophysical Research: Solid Earth*,
725 106(B11), 26561-26591.

726 Li, Z., Liu-Zeng, J., Jia, D., Sun, C., Wang, W., Yuan, Z., & Liu, B. (2016).
727 Quaternary activity of the range front thrust system in the Longmen Shan
728 piedmont, China, revealed by seismic imaging and growth strata. *Tectonics*,
729 35(12), 2807-2827.

730 Li, Z., Liu-Zeng, J., Almeida, R., Hubbard, J., Sun, C., & Yi, G. (2017). Re-evaluating
731 seismic hazard along the southern Longmen Shan, China: Insights from the 1970
732 Dayi and 2013 Lushan earthquakes. *Tectonophysics*, 717, 519-530.

733 Li, Z. W., Tian, B., Liu, S., & Yang, J. (2013). Asperity of the 2013 Lushan
734 earthquake in the eastern margin of Tibetan Plateau from seismic tomography
735 and aftershock relocation. *Geophysical Journal International*, 195(3),
736 2016-2022.

737 Liu, T. K., Hsieh, S., Chen, Y. G., & Chen, W. S. (2001). Thermo-kinematic
738 evolution of the Taiwan oblique-collision mountain belt as revealed by zircon
739 fission track dating. *Earth and Planetary Science Letters*, 186(1), 45-56.

740 Liu, Z., Liang, C., Hua, Q., Li, Y., Yang, Y., He, F., & Fang, L. (2018). The seismic
741 potential in the seismic gap between the Wenchuan and Lushan earthquakes
742 revealed by the joint inversion of receiver functions and ambient noise
743 data. *Tectonics*, 37(11), 4226-4238.

744 Liu-Zeng, J., Zhang, Z., Wen, L., Tapponnier, P., Sun, J., Xing, X., Hu, G., Xu, Q.,
745 Zeng, L., Ding, L. and Ji, C. (2009). Co-seismic ruptures of the 12 May 2008, Ms

746 8.0 Wenchuan earthquake, Sichuan: East–west crustal shortening on oblique,
747 parallel thrusts along the eastern edge of Tibet. *Earth and Planetary Science*
748 *Letters*, 286(3-4), 355-370.

749 Liu-Zeng, J., Wen, L., Oskin, M., & Zeng, L. (2011). Focused modern denudation of
750 the Longmen Shan margin, eastern Tibetan Plateau. *Geochemistry, Geophysics,*
751 *Geosystems*, 12(11).

752 Lu, R., He, D., John, S., Wu, J.E., Liu, B. and Chen, Y., (2014). Structural model of
753 the central Longmen Shan thrusts using seismic reflection profiles: Implications
754 for the sediments and deformations since the Mesozoic. *Tectonophysics*, 630,
755 pp.43-53.

756 Lu, R., Liu, Y., Xu, X., Tan, X., He, D., Yu, G., ... & Wu, X. (2019). Three-
757 dimensional model of the lithospheric structure under the eastern Tibetan Plateau:
758 Implications for the active tectonics and seismic hazards. *Tectonics*, 38(4),
759 1292-1307.

760 Marshak, S. (2004). Salients, recesses, arcs, oroclines, and syntaxes: A review of ideas
761 concerning the formation of map-view curves in fold-thrust belts. In: K. R.
762 McClay ed., Thrust tectonics and hydrocarbon systems, *AAPG Memoir*, 82,
763 131-156.

764 Mazzoli, S., Pierantoni, P. P., Borraccini, F., Paltrinieri, W., & Deiana, G. (2005).
765 Geometry, segmentation pattern and displacement variations along a major
766 Apennine thrust zone, central Italy. *Journal of Structural Geology*, 27(11),
767 1940-1953.

768 Naeser, C. W., Zimmermann, R. A., & Cebula, G. T. (1981). Fission-track dating of
769 apatite and zircon: an interlaboratory comparison. *Nuclear Tracks*, 5(1-2), 65-72.

770 Norris, R. J., & Cooper, A. F. (1997). Erosional control on the structural evolution of a
771 transpressional thrust complex on the Alpine Fault, New Zealand. *Journal of*
772 *Structural Geology*, 19(10), 1323-1342.

773 Pei, S., Zhang, H., Su, J., & Cui, Z. (2014). Ductile gap between the Wenchuan and
774 Lushan earthquakes revealed from the two-dimensional Pg seismic tomography.
775 *Scientific Reports*, 4(1), 1-6.

776 Qin, J., Huh, Y., Edmond, J. M., Du, G., & Ran, J. (2006). Chemical and physical
777 weathering in the Min Jiang, a headwater tributary of the Yangtze River.
778 *Chemical Geology*, 227(1-2), 53-69.

779 Richardson, N. J., Densmore, A. L., Seward, D., Fowler, A., Wipf, M., Ellis, M. A., ...
780 & Zhang, Y. (2008). Extraordinary denudation in the Sichuan Basin: Insights
781 from low-temperature thermochronology adjacent to the eastern margin of the
782 Tibetan Plateau. *Journal of Geophysical Research: Solid Earth*, 113(B4).

783 Royden, L. H., Burchfiel, B. C., King, R. W., Wang, E., Chen, Z., Shen, F., & Liu, Y.
784 (1997). Surface deformation and lower crustal flow in eastern Tibet. *Science*,

785 276(5313), 788-790.

786 Shi, F., He, H. L., & Wei, Z. Y. (2012). Coseismic horizontal shortening associated
787 with the 2008 Wenchuan earthquake along the Baishahe segment from high
788 resolution satellite images. *Journal of Asian Earth Sciences*, 50, p.164-170.

789 Shao, C., Liu, S., Li, Y., Zhou, R., Wang, S., Long, J., ... & Yan, M. (2019).
790 Paleoseismic events on the Shuangshi-Dachuan fault of the seismic gap,
791 Longmen Shan thrust belt, eastern margin of the Tibetan Plateau. *Journal of*
792 *Asian Earth Sciences*, 169, 1-10.

793 Shen, X., Tian, Y., Zhang, G., Zhang, S., Carter, A., Kohn, B., Vermeesch, P., Liu, R.
794 and Li, W., (2019). Late Miocene hinterland crustal shortening in the Longmen
795 Shan thrust belt, the eastern margin of the Tibetan Plateau. *Journal of*
796 *Geophysical Research: Solid Earth*, 124(11), pp.11972-11991.

797 Shen, Z. K., Sun, J., Zhang, P., Wan, Y., Wang, M., Bürgmann, R., ... & Wang, Q.
798 (2009). Slip maxima at fault junctions and rupturing of barriers during the 2008
799 Wenchuan earthquake. *Nature Geoscience*, 2(10), 718-724.

800 Sklar, L. S., & Dietrich, W. E. (2004). A mechanistic model for river incision into
801 bedrock by saltating bed load. *Water Resources Research*, 40(6).

802 Snyder, N. P., Whipple, K. X., Tucker, G. E., & Merritts, D. J. (2000). Landscape
803 response to tectonic forcing: DEM analysis of stream profiles in the Mendocino
804 triple junction region, northern California. *Geological Society of America*
805 *Bulletin*, 112(8), 1250-1263.

806 Sun, C., Jia, D., Yin, H., Chen, Z., Li, Z., Shen, L., et al. (2016). Sandbox modeling of
807 evolving thrust wedges with different preexisting topographic relief: Implications
808 for the Longmen Shan thrust belt, eastern Tibet. *Journal of Geophysical*
809 *Research: Solid Earth*, 121, 4591–4614. <https://doi.org/10.1002/2016JB013013>

810 Sun, C., Li, Z., Zheng, W., Jia, D., Zhang, D., Fan, X., & Zhang, P. (2019). 3D
811 geometry of range front blind ramp and its effects on structural segmentation of
812 the southern Longmen Shan front, eastern Tibet. *Journal of Asian Earth Sciences*,
813 181, 103911.

814 Sun, M., Yin, A., Yan, D., Ren, H., Mu, H., Zhu, L., & Qiu, L. (2018). Role of
815 pre-existing structures in controlling the Cenozoic tectonic evolution of the
816 eastern Tibetan plateau: New insights from analogue experiments. *Earth and*
817 *Planetary Science Letters*, 491, 207-215.

818 Suppe, J. (2007). Absolute fault and crustal strength from wedge tapers. *Geology*,
819 35(12), 1127-1130.

820 Tan, X. B., Lee, Y. H., Chen, W. Y., Cook, K. L., & Xu, X. W. (2014). Exhumation
821 history and faulting activity of the southern segment of the Longmen Shan,
822 eastern Tibet. *Journal of Asian Earth Sciences*, 81, 91-104.

823 Tan, X. B., Xu, X. W., Lee, Y. H., Lu, R. Q., Liu, Y., Xu, C., ... & Kang, W. J. (2017).

824 Late Cenozoic thrusting of major faults along the central segment of Longmen
825 Shan, eastern Tibet: Evidence from low-temperature thermochronology.
826 *Tectonophysics*, 712, 145-155.

827 Tan, X., Yue, H., Liu, Y., Xu, X., Shi, F., Xu, C., Ren, Z., Shyu, J.B.H., Lu, R. and
828 Hao, H., (2018). Topographic loads modified by fluvial incision impact fault
829 activity in the Longmenshan thrust belt, eastern margin of the Tibetan Plateau.
830 *Tectonics*, 37(9), pp.3001-3017.

831 Tan, X., Liu, Y., Lee, Y. H., Lu, R., Xu, X., Suppe, J., ... & Xu, C. (2019). Parallelism
832 between the maximum exhumation belt and the Moho ramp along the eastern
833 Tibetan Plateau margin: Coincidence or consequence? *Earth and Planetary
834 Science Letters*, 507, 73-84.

835 Tapponnier, P., Zhiqin, X., Roger, F., Meyer, B., Arnaud, N., Wittlinger, G., & Jingsui,
836 Y. (2001). Oblique stepwise rise and growth of the Tibet Plateau. *Science*,
837 294(5547), 1671-1677.

838 Tian, Y., Kohn, B. P., Gleadow, A. J., & Hu, S. (2013). Constructing the Longmen
839 Shan eastern Tibetan Plateau margin: Insights from low-temperature
840 thermochronology. *Tectonics*, 32(3), 576-592.

841 Xu, G., & Kamp, P. J. (2000). Tectonics and denudation adjacent to the Xianshuihe
842 Fault, eastern Tibetan Plateau: Constraints from fission track thermochronology.
843 *Journal of Geophysical Research: Solid Earth*, 105(B8), 19231-19251.

844 Xu, X., Wen, X., Yu, G., Chen, G., Klinger, Y., Hubbard, J., & Shaw, J. (2009).
845 Coseismic reverse-and oblique-slip surface faulting generated by the 2008 Mw
846 7.9 Wenchuan earthquake, China. *Geology*, 37(6), 515-518.

847 Xu, X., Wen, X., Han, Z., Chen, G., Li, C., Zheng, W., ... & Wei, Z. (2013). Lushan M
848 S 7.0 earthquake: A blind reverse-fault event. *Chinese Science Bulletin*,
849 58(28-29), 3437-3443.

850 Yin, A., & Harrison, T. M. (2000). Geologic evolution of the Himalayan-Tibetan
851 orogen. *Annual Review of Earth and Planetary Sciences*, 28(1), 211-280.

852 Wang, E., Kirby, E., Furlong, K. P., Van Soest, M., Xu, G., Shi, X., ... & Hodges, K. V.
853 (2012). Two-phase growth of high topography in eastern Tibet during the
854 Cenozoic. *Nature Geoscience*, 5(9), 640-645.

855 Wagner, G., & Van den Haute, P. (2012). *Fission-track dating* (Vol. 6). Springer
856 Science & Business Media.

857 Willett, S.D. (1997). Inverse modeling of annealing of fission tracks in apatite; 1, A
858 controlled random search method. *American Journal of Science*, 297(10),
859 pp.939-969.

860 Wilson, C. J., & Fowler, A. P. (2011). Denudational response to surface uplift in east
861 Tibet: Evidence from apatite fission-track thermochronology. *Bulletin*, 123(9-10),
862 1966-1987.

863 Zheng, G., Wang, H., Wright, T. J., Lou, Y., Zhang, R., Zhang, W., ... & Wei, N.
864 (2017). Crustal deformation in the India-Eurasia collision zone from 25 years of
865 GPS measurements. *Journal of Geophysical Research: Solid Earth*, 122(11),
866 9290-9312.

867 Zheng, Y., Ma, H., Lü, J., Ni, S., Li, Y., & Wei, S. (2009). Source mechanism of
868 strong aftershocks ($M_s \geq 5.6$) of the 2008/05/12 Wenchuan earthquake and the
869 implication for seismotectonics. *Science in China Series D: Earth Sciences*,
870 52(6), 739-753.

871

872 **Figure captions**

873

874 **Figure 1.** Topographic map and neotectonic setting of the Longmen Shan, eastern
875 margin of Tibetan Plateau. Distribution of aftershocks of the 2008 Wenchuan
876 earthquake (red circles) and the 2013 Lushan earthquake (yellow circles) are from
877 Huang et al. (2008) and Fang et al. (2013), respectively. Epicenters (with focal
878 mechanism solutions, if available) for five major earthquakes from Z. Li et al. (2017)
879 and references therein. The aftershock gap is bounded by dark blue dashed lines.
880 Light blue curves denote rivers. Note the relative high topography in the aftershock
881 gap. Surface rupture of the 2008 Wenchuan earthquake from Xu et al. (2009).
882 Abbreviations: BYF, Beichuan-Yingxiu fault; DYF, Dayi fault; JGF,
883 Jiangyou-Guanxian fault; SDF, Shuangshi-Dachuan fault; WMF, Wenchuan-Maoxian
884 fault; WYF, Wulong-Yanjing fault; XPF, Xiongpo fault; XSHF, Xianshuihe fault.

885

886

887 **Figure 2.** (a) Topographic map of the central and southern Longmen Shan, and
888 low-temperature thermochronology data from literature and this study. Data sources:
889 (1) Tan et al. (2017); (2) E. Wang et al. (2012); (3) Kirby et al. (2002); (4) Richardson
890 et al. (2008); (5) Arne et al. (1997); (6) Wilson et al. (2011); (7) Tan et al. (2014); (8)
891 Xu et al. (2000); (9) Tian et al. (2013); (10) Cook et al. (2013); (11) Godard et al.
892 (2009); (12) Shen et al. (2019). (b) Geological map of the central and southern
893 Longmen Shan, and distribution of fluvial shear stress calculations (dark blue lines
894 along rivers). Abbreviations: AFT, apatite fission track; ZFT, zircon fission track; AHe,
895 apatite (U-Th)/He; ZHe, zircon (U-Th)/He; BM, Baoxing massif; PM, Pengguan
896 massif; XM, Xuelongbao massif; SP, Siguniang pluton. For selective period and
897 epoch: Z, Sinian (late Neoproterozoic); T₁₋₂, Lower and Middle Triassic; T₃, Upper
898 Triassic; E, Neogene.

899

900

901 **Figure 3.** Age histograms and radial plots for the AFT samples. For each sample, the
902 pooled age and the number of grains counted are indicated on the histogram.

903

904

905 **Figure 4.** Thermal modeling (left) and track length distributions (right) for DY-07, 08,
906 and 14. In left panel, purple envelope represents good fit paths; green envelope
907 represents acceptable fit paths; black thick line denotes weighted mean path; and
908 black boxes are constraint for modeling. Yellow box highlights the rapid cooling
909 since 8 Ma. Thermal history in grey shadow shall be ignored due to no constraint in
910 the annealing zone. In right panel, green lines denote track length distribution of
911 best-fit modeled thermal history. GOF: Goodness of fit.

912

913

914 **Figure 5.** Close-up view of thermal history from 20 Ma to present, compared with
915 modeled thermal histories with constant denudation rate. Curves of DY-07, 08, and 14
916 are weighted mean paths of their thermal history shown in **Fig. 4**, while those of the
917 DY-01 and 04 are based on the dates and closure temperature. Cooling histories of
918 rocks with denudation rate of 0.3, 0.4, 0.5 and 0.6 mm/yr since 8 Ma are modeled by
919 TERRA software (Ehlers, 2005), with boundary conditions below: surface
920 temperature, 20°C; basal temperature gradient, 25°C/km; maximum model depth, 50
921 km; and diffusivity, $1.3636 \times 10^{-6} \text{ m}^2/\text{s}$.

922

923

924 **Figure 6.** Compilation of river elevation, flood discharge, width, abrasion, and fluvial
925 shear stress with cumulative uncertainty (dark grey area), along the (a) Qingyi Jiang,
926 (b) Yuxi He, (c) Chu He, (d) Xi He, and (e) Shaotang He. The abrasion rates for each
927 formation are from Godard et al. (2010). An index map of rivers and faults in the
928 study area is shown in the lower-right corner.

929

930

931 **Figure 7.** Comparison of basin-averaged fluvial shear stress values and erosion rate
932 from thermochronology measurement. Dashed lines indicate the best linear weighted
933 fits through alluvial sands data for the granitoid crystalline basement (1) and the
934 Paleozoic-Mesozoic sedimentary units (2). The linear fits go through the critical
935 fluvial shear stress value of ~50 Pa. Data point from the hanging-wall block of WMF
936 along the Somang Qu is from Godard et al. (2010). Other data from this study. HW,
937 hanging-wall; FW, footwall.

938

939

940 **Figure 8.** Erosion rates derived from AFT data and modeling (upper panel) and a
941 schematic crustal-scale section X-X' (lower panel) across the aftershock gap. See **Fig.**
942 **2b** for X-X' location. Black points denote AFT samples. Data sources: Xu et al.
943 (2000), Wilson et al. (2011), Tan et al. (2014), and this study. Upper crustal structures
944 are adapted from Hubbard and Shaw (2009) and Z. Li et al. (2017). The Mesozoic
945 Siguniang pluton (SP) is not differentiated from the Precambrian crystalline basement
946 due to unconstrained subsurface boundaries. The partially molten mid-crust (pink)
947 with out-of-plane motion is drawn according to Bao et al. (2020). Thrust faults in the
948 lower crust (grey, dashed lines) are schematic, adapted from Guo et al. (2013) and
949 Feng et al. (2016). Depths of the Moho from Lu et al. (2019). Abbreviations: Cz,
950 Cenozoic; Mz, Mesozoic; Pz, Paleozoic. No vertical exaggeration.

951

952

953 **Figure 9.** Spatial distribution of denudation and topography in the study area. (a)
954 Topographic map and plot of erosion rates along river segments after calibration from
955 **Fig. 7.** (b) Topography profiles (left y-axis) and erosion distribution (right y-axis)
956 along A-A', B-B' and C-C' swath profiles across the Longmen Shan. Green box shows
957 range of average erosion rate inferred from low-temperature thermochronology. Data
958 source: (I) Tan et al. (2017) and Shen et al. (2019); (II) Godard et al. (2009); (III) Tan
959 et al. (2017); (IV) Wilson et al. (2011); (V) and (VI) this study; (VII) Tian et al. (2013)
960 and Tan et al. (2014); (VIII) Cook et al. (2013) and Tan et al. (2014); (IX) Arne et al.

961 (1997). Red line and semi-transparent red box denote average erosion rate from
962 calibration of fluvial shear stress with error range ($\pm 1\sigma$). (c) Topography and erosion
963 rate distribution along the D-D' and E-E' swath profiles (2 km at each side). Dashed
964 and solid thick lines denote variation tendency of erosion and elevation, respectively.

965

966

967 **Figure 10.** Competing models and their predictions for the formation of the
968 aftershock gap. Revised from Y. Liu et al. (in review). (a) Differential wedge strength
969 model. (b) and (c) show patterns of predicted elevation and erosion rate along profiles
970 F-F' and G-G', respectively. As we assume uniform erosion capacity, the erosion rate
971 is positive correlated with the uplift rate. See (a) for profile locations. (d) Differential
972 erosion rate model. (e) and (f) show patterns of predicted elevation and erosion rate
973 along profiles H-H' and J-J' profiles, respectively. See (d) for profile locations.

974

975

976 **Figure 11.** (a) Asperity model. (b) Barrier model. Both revised from Aki (1984).
977 Shaded region is stressed, and blank region is slipped. (c) Sketch map for the active
978 faults and barriers in the central and southern Longmen Shan. Red lines are active
979 faults, and the black lines are inactive or weakly active faults, which act as barrier in
980 earthquakes.

981

Figure 1.

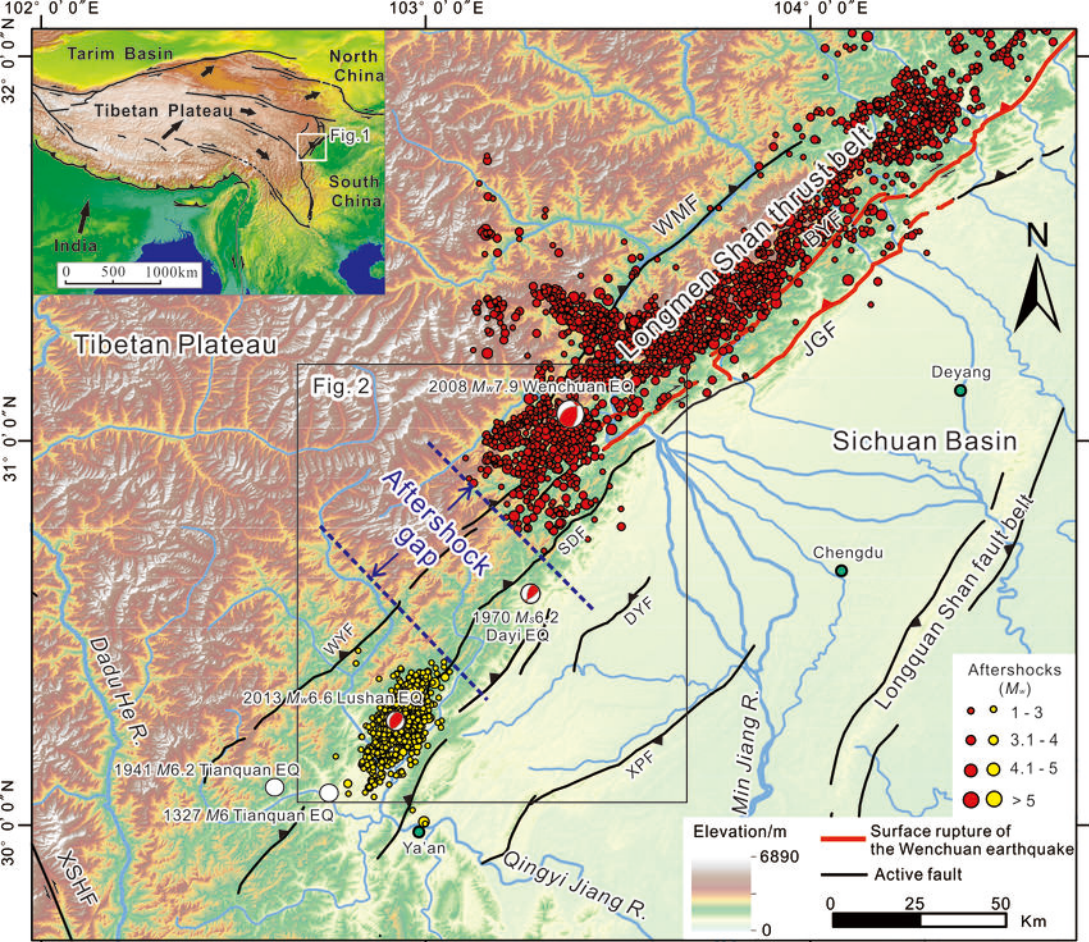


Figure 2.

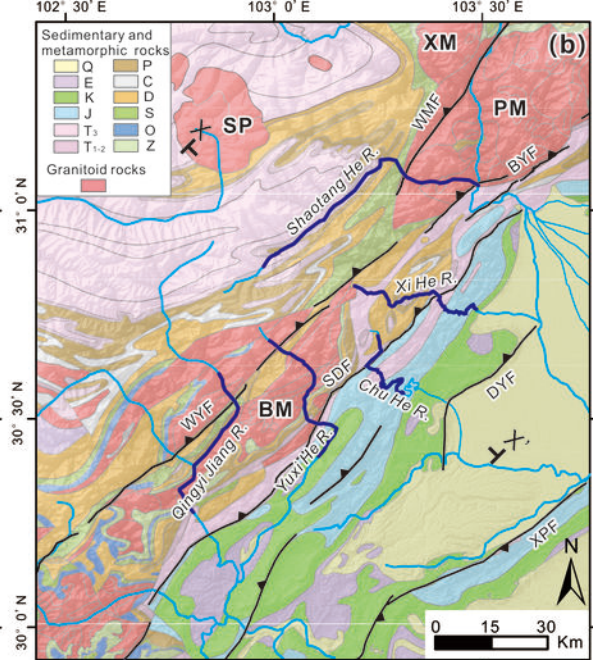
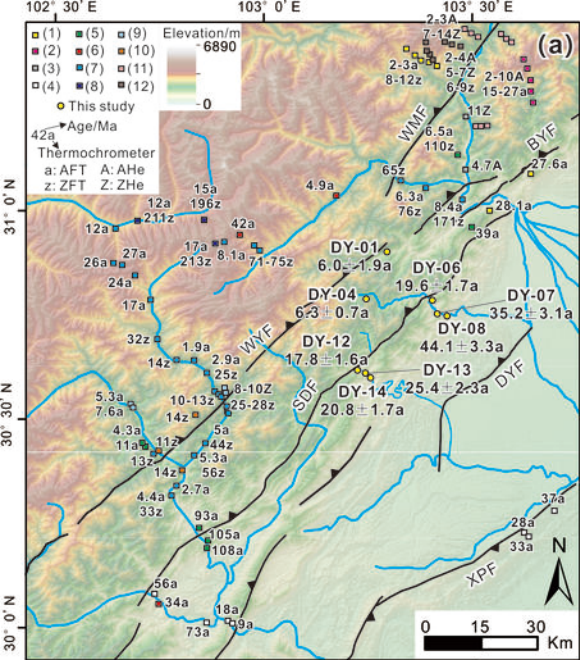


Figure 3.

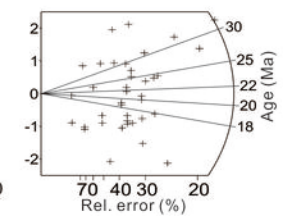
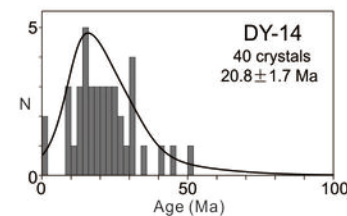
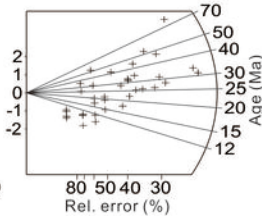
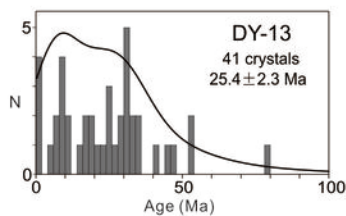
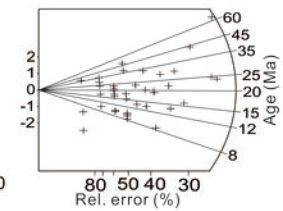
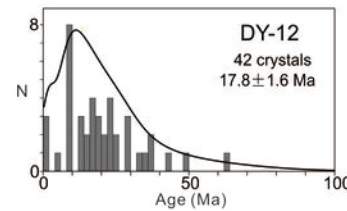
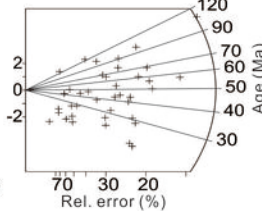
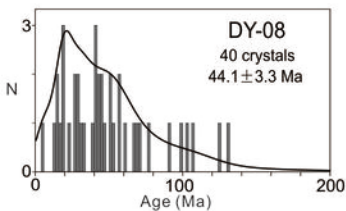
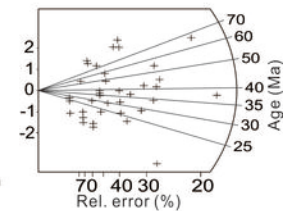
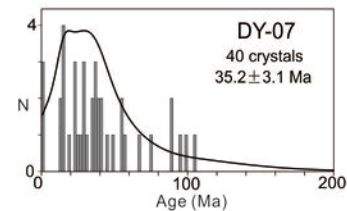
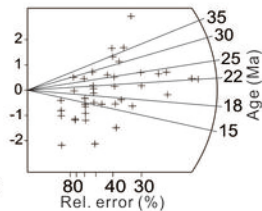
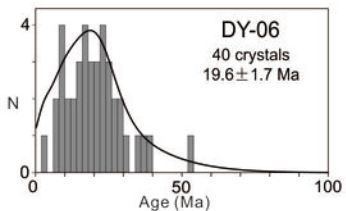
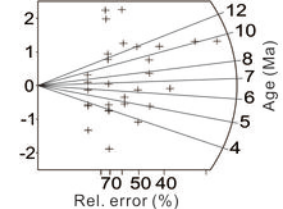
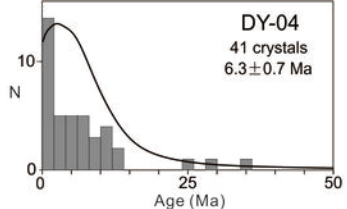
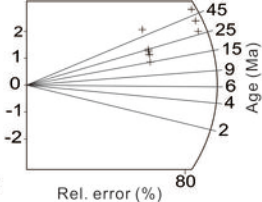
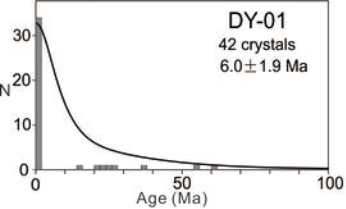


Figure 4.

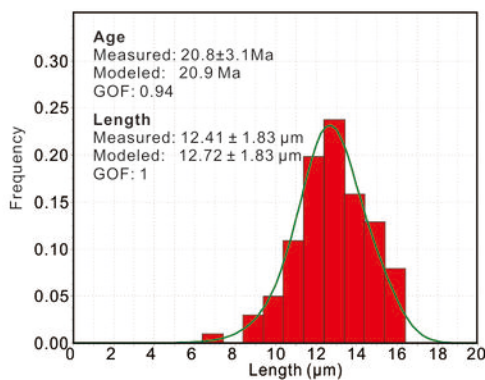
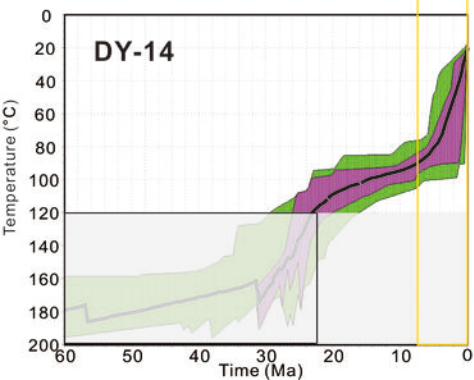
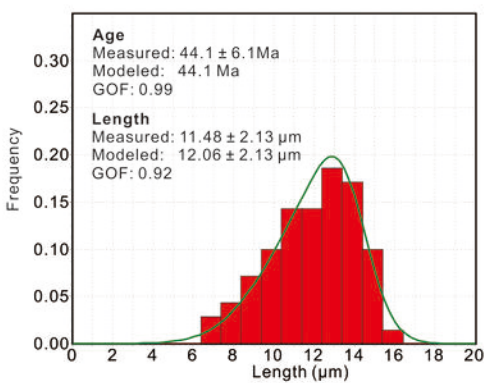
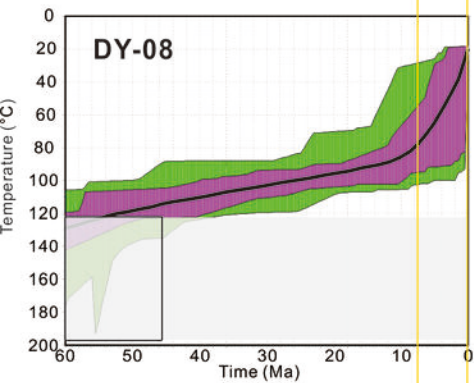
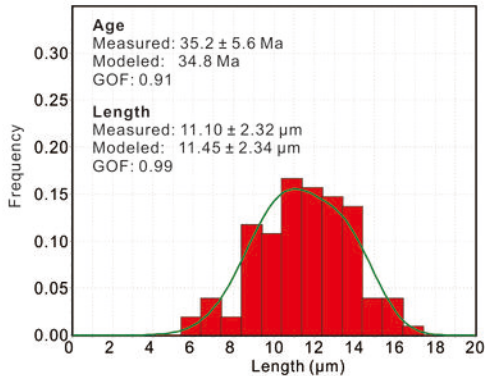
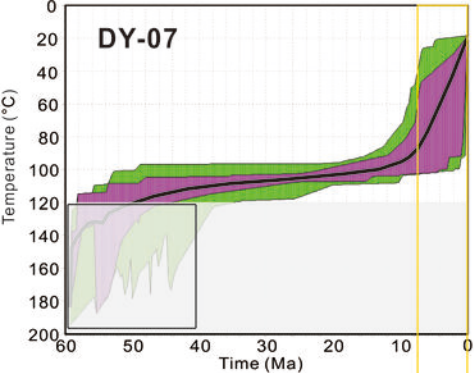


Figure 5.

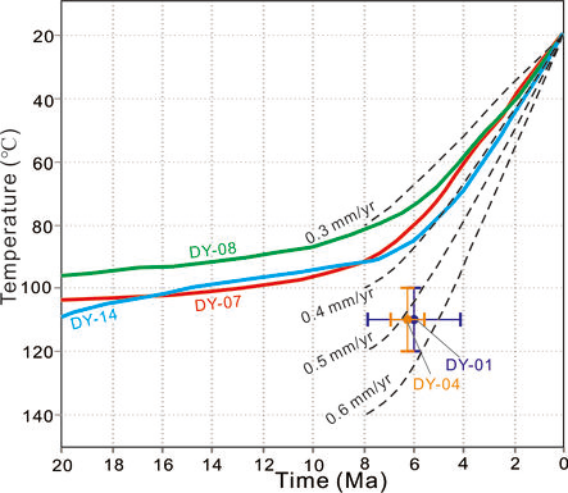
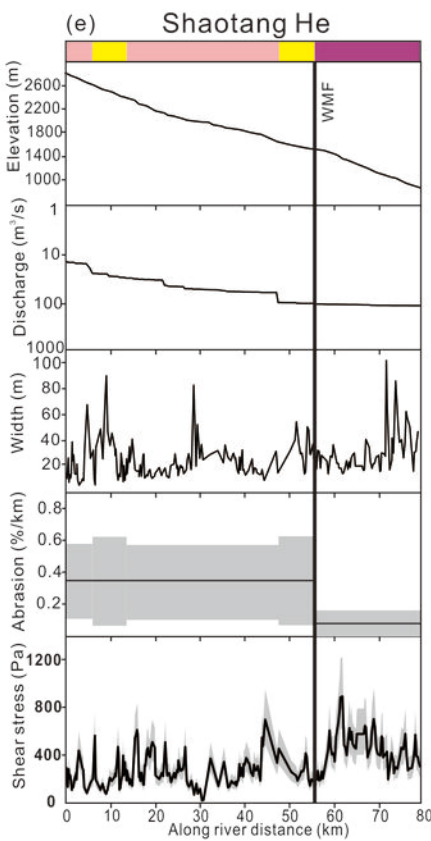
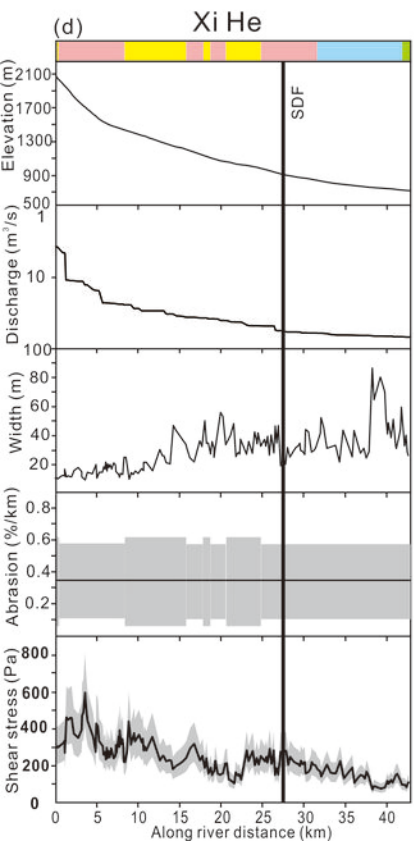
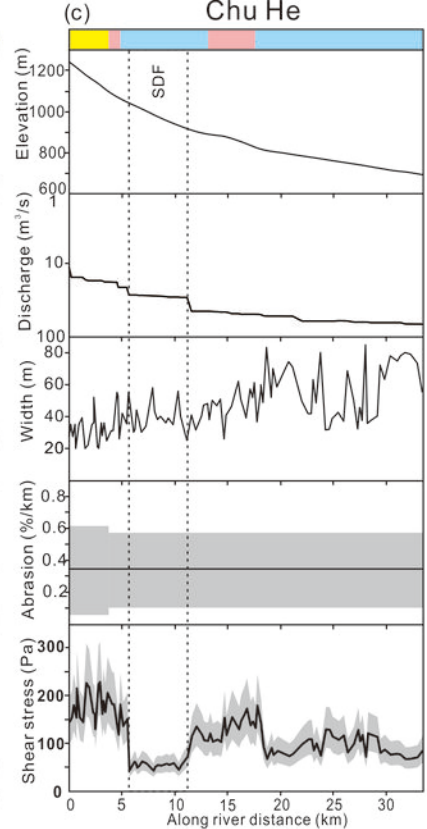
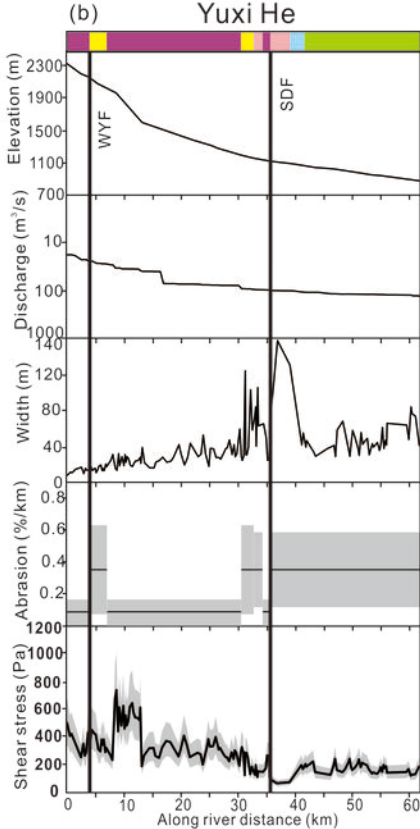
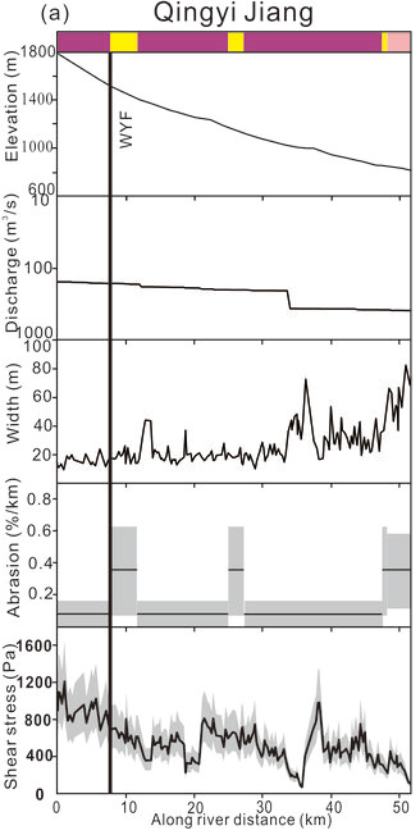


Figure 6.



Legend

- Proterozoic basement
- Paleozoic sedimentary rocks
- Triassic sedimentary rocks
- Jurassic sedimentary rocks
- Cretaceous sedimentary rocks

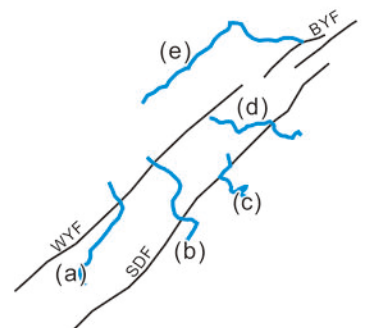


Figure 7.

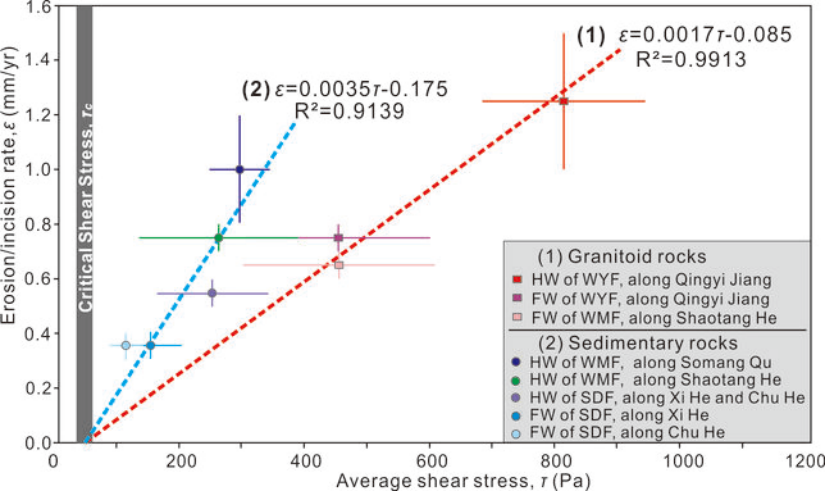


Figure 8.

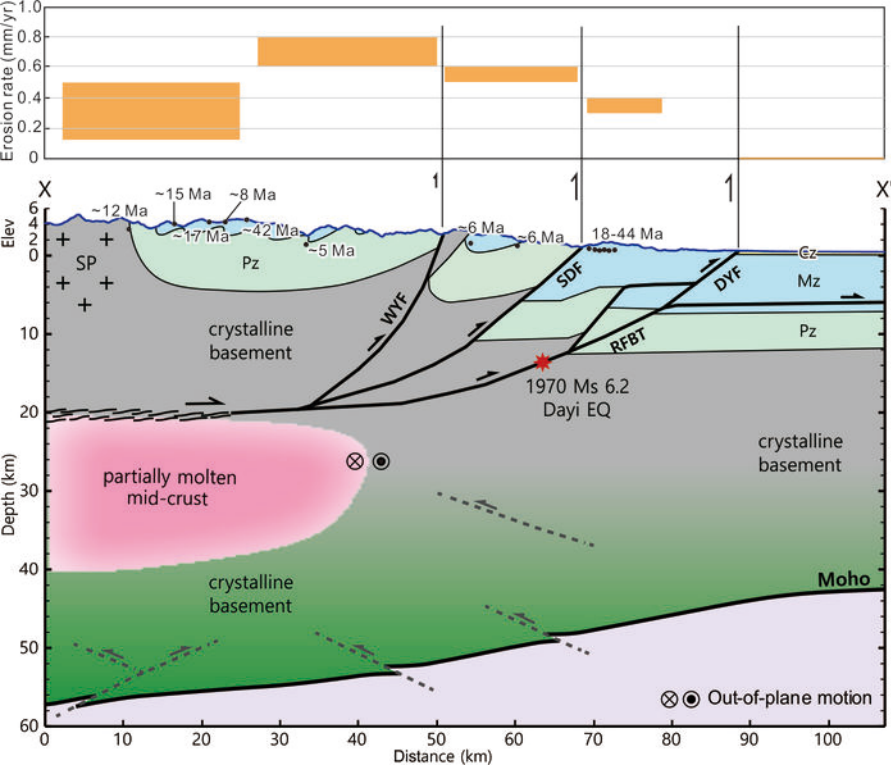


Figure 9.

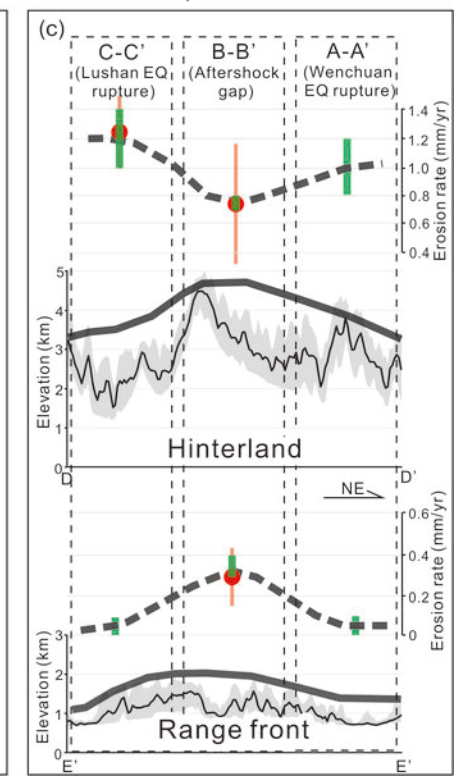
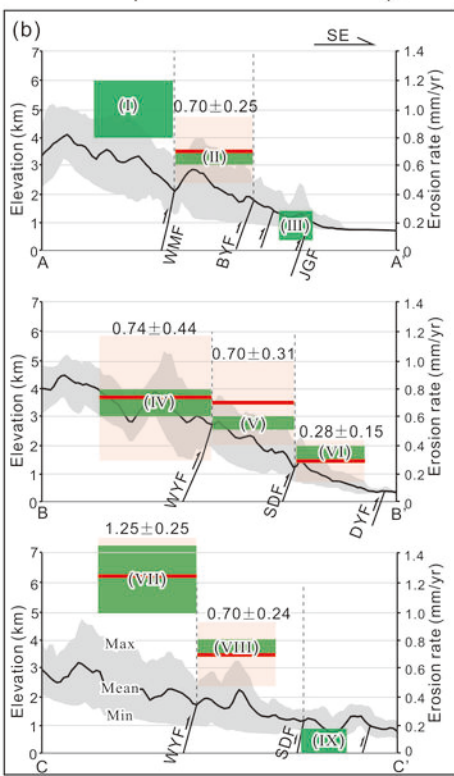
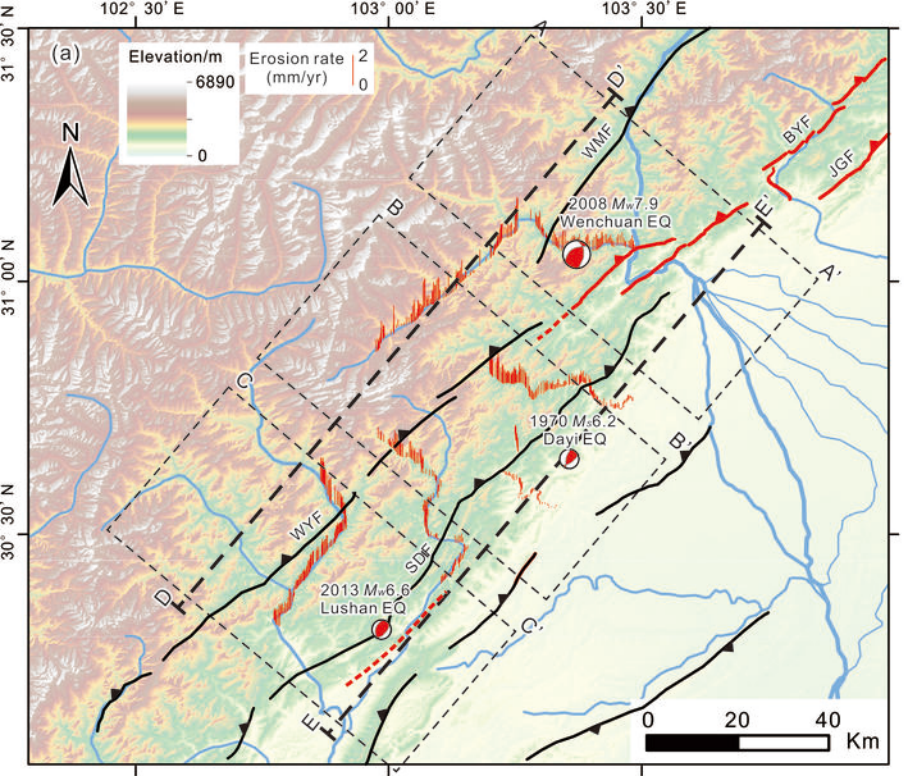
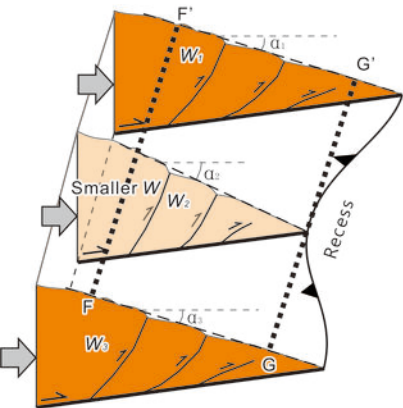


Figure 10.

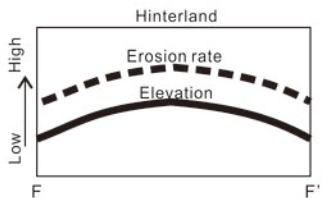
(a) Differential wedge strength (W)

$$W_1 = W_3 > W_2$$

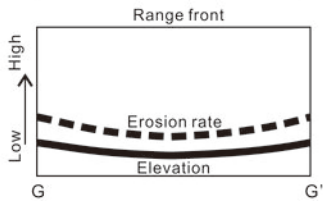
$$\alpha_1 = \alpha_3 < \alpha_2$$



(b)

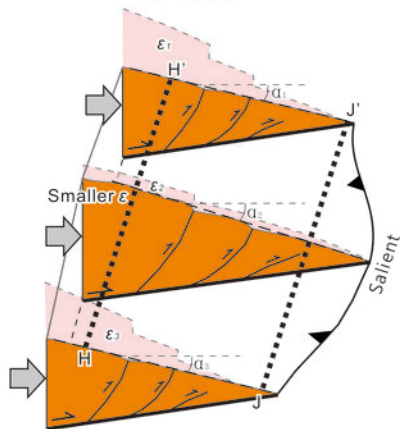


(c)

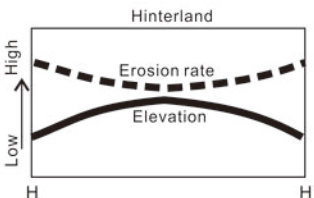
(d) Differential erosion rate (ϵ)

$$\epsilon_1 = \epsilon_3 > \epsilon_2$$

$$\alpha_1 = \alpha_3 < \alpha_2$$



(e)



(f)

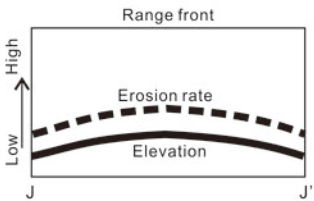
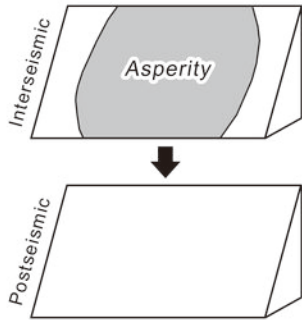


Figure 11.

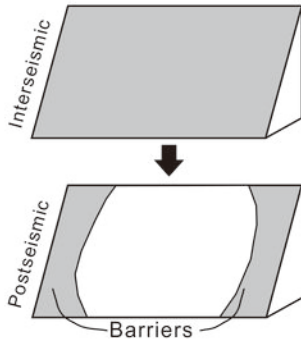
(a)

Asperity model



(b)

Barrier model



(c)

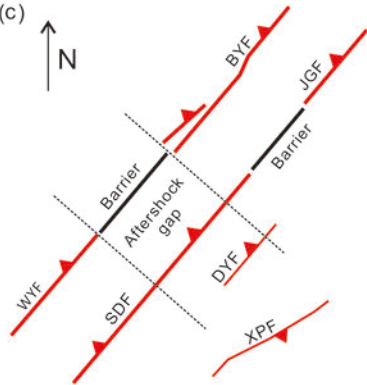


Table 1 AFT data at the aftershock gap of the Longmen Shan.

Sample	Latitude (°N)	Longitude (°E)	Elevation (m)	Lithology	Crystal	RhoS	Ns	RhoI	Ni	RhoD	Nd	P (%)	Age (Ma)
DY-1	30.8956	103.2975	1274	Granitoid	42	0.12	11	6.053	556	17.28	4798	21.76	6.0±1.9
DY-4	30.7825	103.2283	1580	Sandstone	41	0.466	99	22.472	4776	17.28	4798	17.3	6.3±0.7
DY-6	30.7844	103.4031	813	Sandstone	40	1.536	281	20.831	3812	15.25	4798	18.88	19.6±1.7
DY-7	30.7522	103.4222	763	Sandstone	40	1.741	280	14.912	2398	17.28	4798	0.27	35.2±3.1
DY-8	30.7503	103.2183	684	Sandstone	40	3.03	641	18.248	3860	15.25	4798	0	44.1±3.3
DY-12	30.6222	103.2183	919	Sandstone	42	1.037	226	17.513	3818	17.28	4798	0.01	17.8±1.6
DY-13	30.6125	103.23722	849	Sandstone	41	1.685	234	17.662	2453	15.25	4798	0.83	25.4±2.3
DY-14	30.6036	103.25528	845	Sandstone	40	1.827	355	26.493	5149	17.28	4798	14.77	20.8±1.7